Designing Carbon Nitride Modifications for Tuneable CN@Al_2O_3 Supports in Cobalt-catalysed Methanation of CO_2

Angelina Barthelmeß[a], Timo Engl[b], Peter Nagel[c,d], Roland Dittmeyer[b], Michael Rubin[b], Moritz Wolf*[,a,e]

a) Karlsruhe Institute of Technology (KIT), Institute of Catalysis Research and Technology (IKFT), Hermann-von-Helmholtz-Platz 1, 76344 Eggenstein-Leopoldshafen, Germany.

b) Karlsruhe Institute of Technology (KIT), Institute for Micro Process Engineering (IMVT), Hermann-von-Helmholtz-Platz 1, 76344 Eggenstein-Leopoldshafen, Germany.

c) Karlsruhe Institute of Technology (KIT), Institute for Quantum Materials and Technologies (IQMT), Hermann-von-Helmholtz-Platz 1, 76344 Eggenstein-Leopoldshafen, Germany.

d) Karlsruhe Institute of Technology (KIT), Karlsruhe Nano and Micro Facility (KNMFi), Hermann-von-Helmholtz-Platz 1, 76344 Eggenstein-Leopoldshafen, Germany.

e) Karlsruhe Institute of Technology (KIT), Engler-Bunte-Institut (EBI), Engler-Bunte-Ring 1, 76131 Karlsruhe, Germany.

*Corresponding author. E-mail address: moritz.wolf@kit.edu

Abstract

Support materials are often considered as simple stabilising structures for the active phase, yet their physicochemical properties decisively modulate catalyst performance. Carbon nitride (CN) has frequently been combined with metal oxides, predominantly in photocatalysis, where typically only a single bulk-type CN material is employed. Consequently, the influence of different CN morphologies on the structure and catalytic behaviour of CN-modified oxide supports remains largely unexplored. Herein, we establish CN as a tuneable support modification for the Co-catalysed CO_2 methanation by systematically integrating distinct CN morphologies, namely sponge-like (spCN), bulk (bCN), highly porous (hpCN), self-assembled (saCN), and triazine-based (tbCN), onto a conventional Al_2O_3 support via a solution-deposition strategy. This approach yields CN@Al_2O_3 composites with comparable CN loadings (27–31 wt.%) and distinct textural and

chemical properties. Comprehensive characterisation confirms that the surface coverage of Al_2O_3 depends on the morphology of CN, which, in turn, dictates the distribution of Co_3O_4 during decoration with nanoparticles from a separate synthesis. Catalytic testing at 325 °C and 5 bar_g reveals a strong morphology-performance relationship. Co/spCN@Al_2O_3 exhibits the highest productivity with 60% CO_2 conversion and 97% CH_4 selectivity, outperforming composites based on bCN and hpCN or unmodified Al_2O_3 as support material. In contrast, saCN and tbCN modifications resulted in poor performance. Post-run analyses indicate that CN modification enhances interaction with cobalt and mitigates sintering, with the sponge-like morphology providing the most favourable metal-support interactions. These findings demonstrate that CN morphology represents a key design parameter for tailoring metal-support interactions and catalytic performance in thermocatalytic CO_2 hydrogenation.

1. Introduction

Catalytic CO_2 methanation is the fundamental reaction in the Power-to-Gas (PtG) concept and provides a direct route for the conversion of hydrogen from electrolysis of water using renewable energies and captured CO_2 into synthetic natural gas.[1–3] In addition, PtG sparks more and more attention in the framework of chemical energy storage and carbon neutrality. Further, this reaction often serves as a benchmark system in scientific studies to shed light on the relationships between structure and function in heterogeneous catalysis.[2,4,5] The latter motivation is particularly appealing for cobalt-based catalysts due to their intrinsic activity towards the competing formation of CO via the reverse water-gas shift (RWGS) reaction,[6–8] while actual hydrogenation activity is strongly affected by the cobaltous phase formed under reaction conditions.[9–14] Although a wide range of transition-metal catalysts[15] and oxide supports have been investigated, it has become obvious that the support is not merely a passive supporting structure,[16,17] but rather plays an active role in determining the activity, selectivity, and stability of the catalyst by controlling dispersion, defining

active sites, mediating metal-support interactions, or even providing promotional effects by design.[4,5,18]

Research on the role of supports during CO_2 methanation has largely focused on conventional metal oxides, such as Al_2O_3, SiO_2, Y_2O_3, TiO_2, and CeO_2.[1,16,17,19,20] Carbon nitride (CN) has received little attention in thermocatalysis, especially given its well-established use in photocatalysis thanks to its nitrogen-rich framework, electronic tunability, and ability to adopt diverse morphologies.[21–23] The limited application of CN in thermal catalysis arises from practical obstacles as it is typically obtained as a fine powder with low bulk density, which results in severe pressure drops and poor mechanical stability in fixed-bed operations. However, literature provides examples for the multifold use of CN a functional support or modification thereof for thermocatalytic applications, such as the Fischer-Tropsch synthesis,[24–29] CO and CO_2 methanation,[30–35] methanol synthesis[36] and RWGS,[31,36] as well as acetone hydrogenation,[37] where CN-based carriers consistently improve metal dispersion, reducibility, and selectivity for Fe, Co, Ni or Cu-based catalysts. Recently, we have investigated the beneficial modification of an Al_2O_3 support by CN enabling a selective methanation of CO_2 with a Co-based catalyst due to a selectivity switch and activity boost.[35]In the present study, we leverage the morphological diversity of CN by synthesising five distinct pristine CN materials according to literature-established preparation routes, namely bulk (bCN), sponge-like (spCN), highly porous (hpCN), self-assembled (saCN), and triazine-based (tbCN), denoted here according to their dominant structural characteristics. CN has been previously combined with metal oxides,[38] such as TiO_2,[39–42] CeO_2,[43–46] and Al_2O_3,[47–49] to form composite materials. These studies typically employ a single CN material, most commonly bulk-type CN derived from common precursors, i.e. melamine, urea, or dicyandiamide, and focus predominantly on photocatalytic applications.[38] In thermocatalysis, as outlined above, CN-modified catalysts have also been reported, but these studies rarely address how different CN morphologies or structural motifs influence catalytic behaviour when integrated with oxide supports. Equally important, the strategy used to introduce CN onto oxide supports has

received comparatively little systematic attention. In the literature, CN is commonly incorporated either by deposition of pre-formed CN materials or by *in situ* polymerisation of CN precursors in the presence of the oxide support. While both approaches are widely used, they are typically treated as synthetic details rather than as variables that may influence the resulting CN@metal oxide architecture. Direct comparisons are rare,[50–52] although several studies suggest that *in situ* formation can lead to stronger interfacial interactions and more intimate contact between CN and the oxide support compared to deposition of pre-formed CN phases.[52] Consequently, it remains largely unclear how the CN morphology and the pathway of CN formation on the support jointly determine the structure of CN@metal oxide composites and their catalytic behaviour.

To address these questions, pristine CN materials are first prepared and used as reference systems to evaluate how their deposition or in situ formation on Al_2O_3 affects the structure and morphology of CN@Al_2O_3 composites. Different strategies for CN modification of Al_2O_3 are systematically compared, enabling a direct assessment of how the preparation route influences both the structure of the CN phase and the catalytic performance of the resulting materials. All catalysts were subsequently loaded with identical pre-synthesised Co_3O_4 nanoparticles, which allows for decoupling of the influence of the active phase and the support modification. Thus, changes in the catalytic performance can be directly linked to the nature of the CN modification formed on the Al_2O_3 support. By systematically integrating five structurally distinct CN materials onto Al_2O_3 under identical CN loadings and identical active phase conditions, this work establishes CN morphology and the pathway of CN formation on oxide supports as key design parameters governing the structure and catalytic behaviour of CN@Al_2O_3 composites in thermocatalytic CO_2 methanation.

2. Experimental Section

Materials

Cobalt (II) acetate tetrahydrate (98%), γ-alumina (activated, neutral, 100 – 285 mesh, Brockmann Activity I, Fig. S1), and melamine (99%) were obtained from Sigma Aldrich. Benzyl alcohol, acetone, and ethanol were acquired from VWR (Germany). Aqueous ammonia solution (25 wt.%) and cyanuric acid (99%) were supplied by Thermo Scientific. P123 (Pluronic, molecular weight 5800 g mol^{-1}, Sigma Aldrich), potassium chloride (VWR Life Science), and lithium chloride (Acros Organics, 99%) were used as soft-templating agents. Aside from the ammonia solution, which was diluted with deionised water to obtain a concentration of 20 wt.%, all reagents were used as received without further purification.

Preparation of pristine CN materials

bCN: Melamine (66.8 g) was placed in a covered crucible and subjected to thermal treatment at up to 550 °C (Fig. S2).[53] After cool-down, a bright yellow powder was obtained (39.4 g), denoted as bCN.

spCN: Urea (80.4 g) was heated in a covered crucible following the same temperature program (Fig. S2).[54] After cool-down, a light-yellow powder was obtained (5.0 g), denoted as spCN.

saCN: Melamine (15.0 g) was dissolved in 600 mL of dimethyl sulfoxide (DMSO) to form solution A, while cyanuric acid (18.0 g) was dissolved separately in 300 mL of DMSO to form solution B.[55] Solution B was slowly added to solution A under stirring, which immediately resulted in a white precipitate. The suspension was stirred for 30 min and the solid was collected by filtration, washed three times with ethanol (500 mL) and dried to yield 28.2 g of precursor. The dried solid was subsequently heated in a covered crucible in accordance with the same temperature program (Fig. S2) yielding saCN as a beige-yellow fine powder (8.0 g).

hpCN: Pluronic P123 (10 g) was dissolved in 150 g of 2 M HCl and stirred at 35 °C for 13 h at 1700 rpm. Melamine (10 g) and cyanuric acid (10 g) were added and the mixture was stirred for 1 h. The reaction resulted in an opaque dispersion that was maintained by continuous stirring at 35 °C for 24 h, followed by heating to 75 °C and stirring for another 24 h at 1300 rpm. After cooling, the product was filtered, washed three times with warm deionised water (450 mL), dried, and heated according to the standard temperature program (Fig. S2) to yield hpCN.[56,57]

tbCN: A eutectic salt mixture (T_{eut} = 353 °C) of KCl (14.0 g, 56.1 wt.%) and LiCl (11.0 g, 43.9 wt.%) was used as a soft template.[58] Melamine (5.0 g) was mixed with the salt mixture in a crucible and heated according to the same temperature program (Fig. S2). The resulting product was redispersed in warm deionised water (50 °C), filtered, and three times washed with warm water (800 mL) to remove residual salts yielding tbCN.

Thermal treatment: All samples were subjected to a controlled heat treatment in a semi-closed crucible with an initial drying step at 120 °C for 2 h, followed by heating at 2 °C min^{-1} to 500 °C. After a holding time of 2 h to initiate polymerisation, the sample was further heated to 550 °C at 2 °C min^{-1} for polycondensation with a holding time of 2 h (Fig. S2).

Post-treatment: After the thermal treatment, the resulting CN powders (except tbCN) were dispersed in deionised water by stirring in the crucible, filtered using a vacuum pump, three times washed with deionised water (500 mL) to remove residual precursors and ammonia species, and dried overnight at room temperature.

Preparation of CN modified alumina (CN@Al_2O_3)

Three synthesis routes were employed to prepare CN-based composites on Al_2O_3: drop-casting (DC) of pre-synthesised CN, co-calcination (CC) of CN precursors with Al_2O_3 and solution-deposition (SD). DC and CC were only applied for bCN and spCN, whereas all other CN modifications (saCN, hpCN, tbCN) were prepared exclusively via SD.

Drop-casting (DC): A mixture of 2.5 g of pristine CN (bCN or spCN) and 7.5 g of Al_2O_3 was dispersed in 50 mL of deionised water and subjected to a rotary evaporator program for solvent evaporation (Fig. S3). This procedure facilitated the deposition of CN on Al_2O_3 under mild conditions and constant rotation.

Co-calcination (CC): A 30 wt.% loading of CN on Al_2O_3 was obtained by thoroughly mixing the corresponding CN precursor with Al_2O_3 powder in a crucible to ensure maximum homogeneity. For spCN, a mixture of 60.0 g urea and 10.0 g Al_2O_3 was used, while for bCN, 7.0 g melamine and 10.0 g Al_2O_3 were mixed. The prepared samples were transferred to semi-closed crucibles and subjected to the thermal program (Fig. S2).

Solution-deposition (SD): In this approach, Al_2O_3 was impregnated with the respective CN precursors to form intermediate composite precursors. These impregnated Al_2O_3 samples were subsequently subjected to the standard thermal treatment (Fig. S2) to form the corresponding CN@Al_2O_3 composites, followed by washing according to the procedures applied during synthesis of the corresponding pristine CN.

bCN@Al_2O_3_SD: 15.0 g of melamine was dissolved in 350 mL of deionised water in a 500 mL beaker and magnetically stirred at 65 °C for 15 min. A total of 14.0 g of Al_2O_3 was added, followed by an additional 30 min of stirring.[25] Water was evaporated by heating to 120 °C on a hot plate under continuous stirring. Once the volume was reduced by half, the mixture was transferred into a crucible while stirring was continued. A white slurry that solidified upon cooling to room temperature was obtained. The sample was then subjected to the thermal treatment (Fig. S2).

spCN@Al_2O_3_SD: A total of 60.0 g of urea was dissolved in 200 mL of deionised water in a 500 mL beaker and magnetically stirred at 65 °C for 15 min. Under continuous stirring for another 30 min, 10.3 g of Al_2O_3 was added. Water was evaporated by heating to 120 °C under continuous stirring. When the volume was reduced by half, the mixture was transferred into a crucible, which yielded a white slurry that solidified upon cooling to room temperature. The sample was then subjected to the thermal treatment (Fig. S2).

saCN@Al_2O_3_SD: Melamine (10.0 g) was dissolved in 400 mL DMSO at 80 °C (solution A) and cyanuric acid (12.0 g) was dissolved separately in 200 mL of DMSO at 80 °C (solution B). To each solution, 4.0 g of Al_2O_3 was added, followed by 30 min of stirring at 650 rpm. Solution A was then poured into solution B, immediately forming a white precipitate. The suspension was stirred for 12 h at room temperature. The resulting solid was collected by vacuum filtration using a Büchner funnel, washed three times with ethanol (500 mL), dried, and subsequently subjected to the thermal treatment (Fig. S2).

hpCN@Al_2O_3_SD: Pluronic P123 (2.0 g) was dissolved in 30.0 g of 2 M HCl and stirred at 35 °C for 13 h at 700 rpm. Melamine (2.2 g) and cyanuric acid (2.2 g) were added and the mixture was stirred for 1 h, while turning opaque. Al_2O_3 (2.6 g) was added and the mixture was maintained at 35 °C for 24 h, followed by heating to 75 °C and stirring for another 24 h at 750 rpm. After cooling, the product was filtered, washed three times with warm deionised water (450 mL), dried, and heated according to the standard program (Fig. S2).

tbCN@Al_2O_3_SD: Melamine (10.0 g), LiCl (21.97 g) and KCl (28.06 g) were dissolved in 350 mL of deionised water in a 500 mL beaker and magnetically stirred at 65 °C for 15 min. A total of 9.7 g of Al_2O_3 was added, followed by an additional 30 min of stirring. Water was evaporated by heating to 120 °C under continuous stirring. Once the volume was reduced by half, the mixture was transferred into a crucible while stirring was continued, resulting in a white slurry that solidified upon cooling to room temperature. The sample was then subjected to the thermal treatment (Fig. S20).

Synthesis of Co_3O_4 nanoparticles

Co_3O_4 nanoparticles were synthesised via the benzyl alcohol route, a solvent-controlled thermal treatment without the use of classical surfactants,[59–62] following a modified method reported in literature.[60] A total of 3.2 g of cobalt(II)acetate tetrahydrate was dissolved in 100 mL of benzyl alcohol under magnetic stirring using a round-bottom flask placed in an aluminium heating block

with a set temperature of 70 °C. While vigorous stirring was maintained, 130 mL of a 20 vol.% aqueous ammonia solution were added dropwise to the dark purple solution, which resulted in the formation of a brown emulsion. When the pH, determined using universal indicator paper, reached 12, the flask was immediately transferred into an oil bath preheated to 175 °C for flash heating of the reaction mixture. The suspension was kept at this temperature under stirring for 3 h for aging and then allowed to cool down to room temperature under continuous stirring. For washing of the nanoparticles, 100 mL of diethyl ether was added to the mixture and the resulting dispersion was centrifuged in 45 mL tubes at 7830 rpm for 30 min. The obtained solid was redispersed in 15 mL of ethanol using ultrasonication, followed by the addition of 30 mL of acetone to induce flocculation followed by a second centrifugation. The washing steps were repeated once. The resulting nanoparticles were collected and dried in a fume hood under ambient conditions.

Catalyst preparation

The parent catalysts were prepared by decoration of support (composites) with pre-synthesised Co_3O_4 nanoparticles.[10,63] The corresponding amount of Co_3O_4 nanoparticles for a final loading of 3.2 wt.% was dispersed in 25 mL of ethanol using ultrasonication, while the required quantity of support material was added to 150 mL of ethanol in a round-bottom flask. Both dispersions were ultrasonicated for 1.5 h, while the support slurry was additionally stirred mechanically using an overhead stirrer to prevent settling. The nanoparticle dispersion was added dropwise to the support suspension under continuous ultrasonication and mechanical overhead stirring. After 2 h, the mixture was transferred to a rotary evaporator for solvent removal (Fig. S3). The resulting catalyst powders were sieved and the 20 – 106 µm size fraction was used for characterisation and catalytic testing in the fixed-bed reactor.

Characterisation techniques

Scanning electron microscopy (SEM) was performed using a Zeiss GeminiSEM 500 with a thermal Schottky field emitter cathode. In addition to an Everhart-Thornley and InLens secondary electrons

detectors an in-column energy selective backscattered (ESB) detector was used. Samples were placed on carbon tape on standard aluminium SEM pin stub mount, Ø12.7mm x 8mm pin height.

X-ray diffraction (XRD) was conducted using an X'Pert PRO diffractometer (PANalytical) operating at 40 kV and 40 mA using a Ni filtered Cu Kα radiation source (λ = 0.15406 nm). The patterns were acquired in a 2θ scanning range from 5° to 80° with a step size of 0.017° and a total scan time of 2 h. Obtained XRD patterns were compared to reference patterns of the Powder Diffraction File of the Crystallography Open Database (COD ID; Co_3O_4: 1538531, fcc-Co: 9008466, Al_2O_3: 2015530). Diffraction line broadening analysis via the Scherrer equation (Co_3O_4: (311) diffraction) with correction for the instrumental line broadening and a shape factor of 0.9 was applied to estimate the crystallite size of the Co_3O_4 nanoparticles.

For N_2 adsorption-desorption isotherms, the samples were degassed at 250 °C for 12 h. N_2 physisorption was conducted at −196 °C (liquid N_2) using a Quantachrome Nova 2000 instrument. The specific surface areas and pore structure of the materials were approximated according to the Brunauer-Emmett-Teller (BET) and Barrett-Joyner Halenda (BJH) methods, respectively.

Fourier-transform infrared (FTIR) spectra were recorded using an INVENIO R spectrometer (Bruker) equipped with a Specac Golden Gate single-reflection attenuated total reflection (ATR) accessory with a diamond crystal. Samples were placed directly onto the ATR crystal without any further preparation. Spectra were collected in the range of 4000 – 400 cm^{-1} with a spectral resolution of 1 cm^{-1} and 64 scans were averaged for each measurement.

A TGA 2 analyzer (Mettler Toledo) was used to study CN@Al_2O_3 composites by means of thermogravimetric analysis (TGA). Approx. 2 mg of the sample was placed in a 70 µL alumina crucible and continuously heated from 25 to 1000 °C at a heating rate of 10 °C min^{-1} under a flow of 50 mL min^{-1} of synthetic air. The amount of CN in CN@Al_2O_3 samples was determined as the weight loss after removal of volatile compounds, i.e. the difference between the final weight after decomposition/oxidation of CN and the weight during the ramp at 250 °C.

The Raman spectroscopic investigations were carried out using an inVia Reflex spectrometer system (Renishaw) with an excitation laser operating at a wavelength of 785 nm. The spectra were recorded in the range from 64 to 3433 cm^{-1}. A grating with 1800 lines mm^{-1} was used for spectral dispersion. A 50× objective was used for the *ex situ* measurements. Raman spectra were recorded at five spatially separated measurement points per sample. Five accumulations were performed at each measurement point, with the intensities from five repeat measurements summed to improve the signal-to-noise ratio. Cobalt loadings were determined using optical emission spectrometry with inductively coupled plasma (ICP-OES). The measurement was carried out using an Agilent 725 (Agilent Technologies). For this purpose, the catalysts were dissolved in a volumetric 3:1 mixture of HNO_3 and HCl and digested using a microwave. The solutions were atomised in argon plasma gas and the emitted light was measured radially. By analysing the characteristic wavelength of this light, the concentration of the elements in the solution could be determined.

^{13}C MAS and CP/MAS NMR measurements were conducted on a JEOL JNM-ECZ400R spectrometer, equipped with a 9.4 T Oxford cryo-magnet, using a 3.2 mm Jeol Automas Solid State Probe head. ^{13}C MAS MNR spectra were recorded at a resonance frequency of 100.556 MHz with a sample spinning frequency of 14 kHz using the standard “single_pulse_dec_solid.jxp” sequence delivered with the Delta 5.3.3 Software (Jeol). The decoupling was run using Two Pulse Phase Modulation (TPPM, pulse width - Irr_Pwith- of 2.9 µs). 4096 scans were accumulated upon single pulse excitation with 2.2 µs pulse width and 5 s relaxation delay (repetition time: 5.04063 s: X_Acq_time: 40.6323 ms + Relax. Delay). ^{13}C CP/MAS NMR spectra were recorded using the same spinning speed and frequency with the standard “cpmas.jxp” sequence and an optimised contact time (2.5 ms, optimised performing an arrayed experiment with value ranging from 0.8 ms up to 2.5 ms). 4096 scans were accumulated upon single pulse excitation with 2.2 µs pulse width and 4 s relaxation delay (repetition time: 4.03244: X_Acq_time: 32.4403 ms + Relax. Delay). The

^{13}C chemical shifts were calibrated relative to TMS (tetramethylsilane), hexamethyl benzene (Csp^2 δ = 131.82 ppm Csp^3 δ = 16.97 ppm).

X-ray photoelectron spectroscopy (XPS; SPECS Phoibos 150 analyzer) of the heptazine based CN materials was performed using a non-monochromatic XR-50 Mg Kα X-ray source, with an incident angle of 45° between the analyser and the X-ray source. The energy scale was calibrated using a silver reference. To minimise charging effects, a flood gun was employed and the samples were placed on silver tape. The survey spectra were measured with a pass energy of 50 eV and a step size of 0.5 and the high-resolution scans with a pass energy of 20 eV and a step size of 0.03. Data analysis was carried out with the CasaXPS software. Peak fitting of the N1s and C1s regions was conducted using a mixed Gaussian-Lorentzian (GL(30)) line shape and a Shirley-type background. A consistent full width at half maximum (FWHM) was applied to all component peaks within each spectrum (N1s: bCN 1.57 eV, spCN 1.59 eV, saCN 1.82 eV; C1s: bCN 1.66 eV, spCN 1.67 eV, saCN 1.73 eV).

Soft X-ray absorption spectroscopy (sXAS) at the N K-edge was performed at the WERA beamline at the Karlsruhe Research Accelerator (KARA), KIT Light Source, Germany. Spectra were recorded at room temperature in total electron yield (TEY) mode with a photon energy resolution of 0.22 eV and a degree of linear polarisation of 95%. The energy scale was calibrated by comparison to sXAS from a NiO reference measured in parallel. Data processing was carried out by division by the primary intensity I_0, background-subtraction, and normalisation at an energy around 423 eV.

Diffuse reflectance UV-vis (DRS UV-vis) spectra were recorded using a JASCO V-650 spectrophotometer equipped with a Harrick Praying Mantis™ diffuse reflectance accessory. Samples were measured in 10 mm precision quartz cuvettes without further preparation. Spectra were collected over the desired UV-vis range using $BaSO_4$ as the reflectance standard.

Diffuse reflectance data were converted to Kubelka-Munk units for evaluation of optical properties, and band gaps were derived by Tauc plot analysis assuming the appropriate electronic transition type.

Diffuse Reflectance Infrared Fourier Transform Spectroscopy (DRIFTS)

The set-up used for the DRIFTS measurements is a channel-type reactor with optical access referred to as spatially resolved DRIFTS reactor. The key characteristics are described in the following, a more detailed description can be found in previous publications.[64,65] The reaction chamber is divided in five reaction zones, each hosting one microstructured foil with the dimensions of 22 x 24 mm coated with the catalyst. The Co/spCN and Co/spCN@Al_2O_3 catalysts were studied using DRIFTS. The coating procedure of the micro-structured foils with catalyst powder has been described in detail in Engl *et al*.[64] For each catalyst, five catalyst plates were screen printed (Co/spCN: $m_{catalyst}$ = 7.9, 5.7, 13.3, 13.6, 13.5 mg, m_{total} = 54.0 mg and Co/spCN@Al_2O_3: $m_{catalyst}$ = 21.7, 9.6, 12.3, 11.8, 11.7 mg, m_{total} = 67.1 mg) and placed in the reactor. The catalyst was *in situ* reduced in 50% H_2/N_2 for 8 h at 400 °C under atmospheric pressure at a flow rate of 300 mL min^{-1}. After reduction, the reactor was purged with N_2 (99.999 vol.%) and pressurised to 5 bar_g. A CaF_2 window on top of the reactor allows for light, especially infrared radiation to enter and leave the reactor allowing for DRIFTS analysis. As a radiation source an IR cube FT-IR OEM spectrometer with a resolution of 4 cm^{-1} from Bruker Optics was used to generate IR radiation in a wave number range from 4000 to 1150 cm^{-1} (liquid N_2 cooled MCT (Mercury Cadmium Telluride) detector). Before the analysis of the catalyst during CO_2 methanation, background spectra were measured for each temperature to subtract the contribution of the mirrors, spectrometer, and other factors from the sample spectrum allowing for investigating the effects of species involved in the methanation reaction. For the acquisition of the background spectra, a slightly reducing atmosphere is used (10% H_2/N_2) at 5 bar_g. The spectra are averaged over 40 single measurements to minimise noise.

CO_2 methanation experiments

CO_2 methanation was performed in a tubular fixed-bed reactor with an internal diameter of 6.5 mm. To minimise temperature gradients caused by the highly exothermic CO_2 methanation reaction, 0.375 g of catalyst (particle size 20–106 µm) was diluted with 1.125 g of SiC (106–140 µm) in a mass ratio of 1:3. The homogenous mixture was loaded into the isothermal zone of the reactor, and placed between two quartz wool plugs. The fixed-bed reactor setup and instrumentation have been described in detail in our previous work.[35] The reaction temperature was monitored using a thermocouple positioned directly inside the catalyst bed, while three additional thermocouples located along the outer reactor wall were used for temperature control. No measurable temperature difference between the internal and external thermocouples was observed for any experiment at any time during operation. For the *in situ* reduction in Zone I, the catalyst was heated to 200 °C at 4 °C min^{-1} with a holding time of 15 min, and further heating to 350 °C at 2 °C min^{-1} for 2 h under a flow of 35.6 mL min^{-1} of 45% H_2/Ar. Subsequently, the system was allowed to cool down to 150 °C under a flow of Ar (Zone II). After a 1 h holding time under 5 bar_g with a feed gas of $H_2/CO_2/Ar$ = 72/18/10, the reactor was heated to 325 °C at 2 °C min^{-1} in Zone III. CO_2 methanation was carried out in Zone IV at 325 °C and 5 bar_g for 9 h (TOS of 0 – 9 h) using a total flow rate of 35.6 mL min^{-1} corresponding to a GHSV of 5.7 L h^{-1} g^{-1}. Finally, the reactor was allowed to cool down to room temperature under an Ar flow (Zone V) and the reactor was opened to enable diffusion-controlled passivation of the catalyst by ambient air.[66] Throughout the run, the effluent gas of the reactor was analysed by an online μ-GC Fusion Gas Analyzer system equipped with TCDs (Inficon).

The catalytic performance of the catalysts was assessed based on the conversion of CO_2 and H_2 (X_{CO_2}, X_{H_2}) as well as selectivity towards CH_4 and CO (S_{CH_4}, S_{CO}), which are calculated according to equations (1) and (2), respectively.[67]

$$X_k = \frac{n_{k,in} - n_{k,out}}{n_{k,in}} \cdot 100\% \quad (1)$$

$$S_i = \frac{n_{i,out}}{\sum n_{products}} \cdot 100\% \quad (2)$$

where, $n_{k,in}$ and $n_{k,out}$ are the molar flow rates of CO_2 or H_2 at the reactor inlet and outlet, respectively, $n_{i,out}$ is the molar flow rate of methane or CO at the reactor outlet, and $n_{products}$ is the total molar flow of all products combined at the reactor outlet.

The rate-normalised metrics, namely the methane space–time yield ($\mathrm{STY_{CH_4}}$) and the CO_2 consumption rate ($\mathrm{r_{CO_2}}$) are defined according to equations (3) and (4):

$$STY_{CH_4} = \frac{n_{CH_4,out}}{m_{Co}} \quad (3)$$

$$r_{CO_2} = \frac{n_{CO_2,in} - n_{CO_2,out}}{m_{Co}} \quad (4)$$

3. Results

3.1 Material Synthesis: From Control over CN Morphology to Al_2O_3 Modification

3.1.1 Pristine CN Morphologies and Structures

While all CN materials were synthesised via thermal polycondensation at 550 °C, systematic variation of the precursor chemistry and templating strategy yielded distinct morphological and textural properties. SEM imaging (Fig. 1a–e, Fig. S4) and N_2 physisorption (Fig. 1f, Fig. S5) reveal a broad range from dense bulk structures to increasingly open frameworks with template-induced mesoporosity and hierarchical organisation. Bulk CN (bCN), obtained by conventional melamine condensation,[53] exhibits a dense morphology with minimal surface roughness, negligible porosity, and a low specific surface area of 8 $m^2\ g^{-1}$. Substituting melamine with urea produces a sponge-

like carbon nitride (spCN) featuring an open, foam-like network of interconnected lamellar domains and abundant voids[54,68] with a moderately increased specific surface area of 39 m^2 g^{-1}. A type IV isotherm with pronounced H3 hysteresis suggests slit-shaped mesopores formed by sheet-like aggregates,[32,69] which also reflects in a broad pore size distribution extending into the macropore range (Fig. S5).

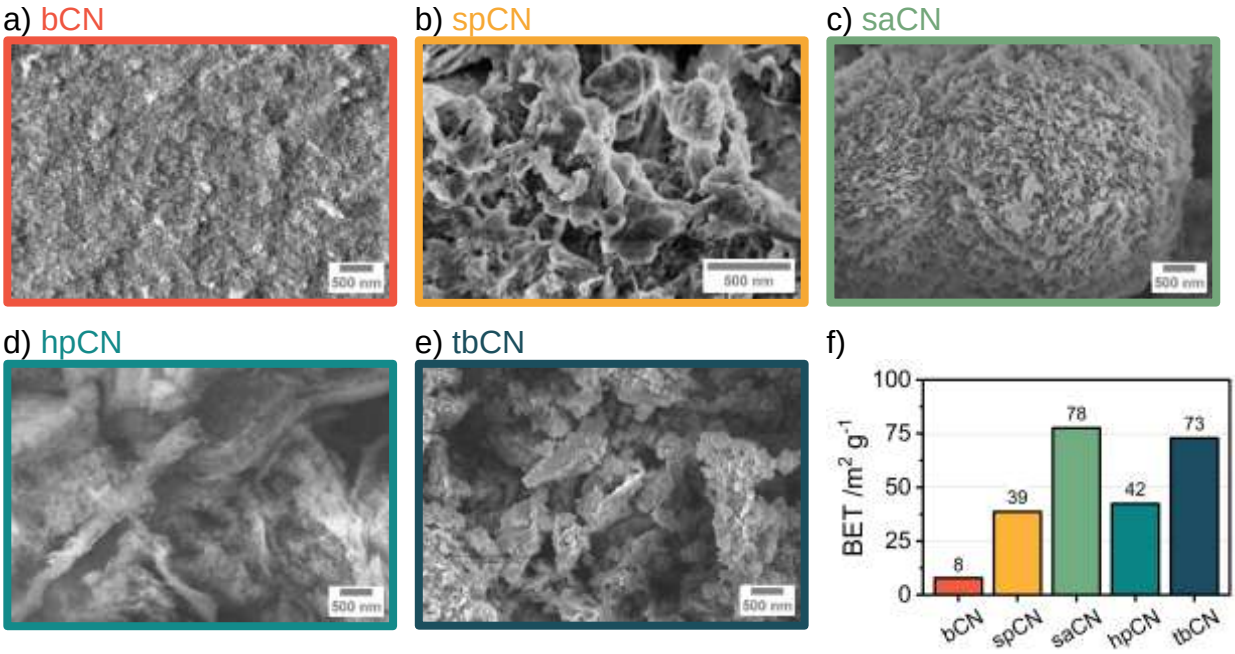

Fig. 1 Morphology and surface area of CN materials. a – e) SEM images of bCN, spCN, saCN, hpCN, and tbCN. f) Specific surface areas obtained from N_2 physisorption measurements.

The self-assembled CN (saCN), obtained from melamine and cyanuric acid through hydrogen-bond-directed supramolecular organisation in DMSO, represents spherical superstructures composed of radially arranged nanosheets.[55] The resulting hierarchical porosity with H3/H4 hysteresis indicates a large number of small mesopores (Fig. S5), which results in the highest BET surface area of 78 m^2 g^{-1}.[55] To exert more control over pore generation within the same precursor system, the synthesis was adapted to an aqueous route using Pluronic P123 as a soft structure-directing agent.[56,57] The resulting highly porous CN (hpCN) preserves the nanosheet-based framework, but develops a more open and uniformly connected mesopore network. After template removal, SEM reveals loosely stacked sheets with enlarged interlayer spacing, while N_2

physisorption confirms a narrower mesopore size distribution than spCN (Fig. S5). This tailored pore architecture leads to an increased BET surface area of 42 m^2 g^{-1}.

To establish a more versatile reaction environment, the synthesis was also transferred into a molten-salt system based on a LiCl/KCl eutectic mixture.[58,70] This melt is thermally stable and chemically inert with a melting point below the polymerisation threshold of s-heptazine. In such an ionic environment, the small molecular precursors and their intermediate oligomers are efficiently solvated, allowing for controlled condensation of the CN framework. The molten phase thereby serves as a confined reaction space that limits extensive layer stacking and promotes the formation of fragmented, plate-like CN domains with irregular surface features and voids.[71,72] The resulting triazine-based CN (tbCN) has a high BET surface area of 73 m^2 g^{-1}, which reflects the pronounced textural evolution during salt-mediated condensation, while the polymerisation pathway shifts from conventional heptazine-based condensation (Fig. 2c) toward a triazine-linked network (Fig. 2d) reminiscent of polytriazine imide (PTI) type structures formed in ionic media.[70,73,74]

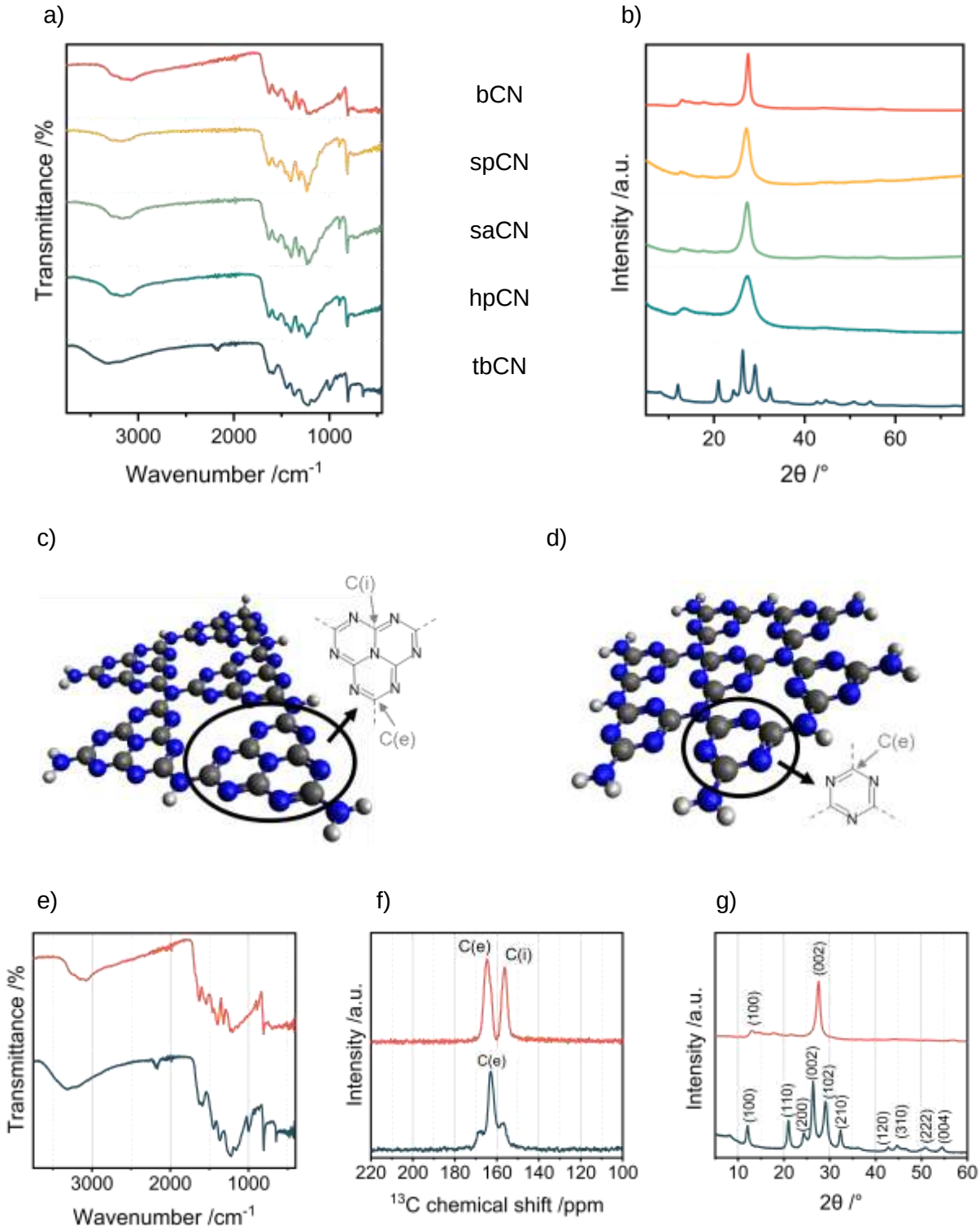

Fig. 2 Structural characterisation of CN materials. a) ATR-FTIR spectra and b) XRD patterns of bCN, spCN, saCN, hpCN, and tbCN. Molecular structures illustrating c) the heptazine and d) triazine building blocks in the CN framework. Comparison of bCN (red) representing heptazine-based materials and tbCN (blue) by e) ATR-FTIR, f) ^{13}C CP/MAS NMR, and g) XRD.

ATR-FTIR spectroscopy (Fig. 2a) reveals that bCN, spCN, saCN, and hpCN exhibit the characteristic vibrational fingerprint of heptazine-based CN. All four materials display the typical stretching vibrations of conjugated C–N=C and C–N–C linkages in the range 1200 – 1650 cm^{-1} together with the heptazine ring-breathing mode at approximately 800 cm^{-1}.[48] Weak N–H stretching bands in the region 3000 – 3400 cm^{-1} indicate residual terminal amine groups consistent with incomplete condensation.[55,75] In contrast, the ATR-FTIR spectrum of tbCN (Fig. 2a, e) features vibrations absent in the heptazine-based CN samples. The bands at 1585, 1153, 993, and 640 cm^{-1} are consistent with PTI-like structures and indicate the presence of triazine-based structural motifs.[72] The reduced intensity of N–H vibrations together with the appearance of a broad O–H component between 3200 and 3600 cm^{-1} suggests a higher degree of condensation alongside an increased interaction with coordinated or surface-bound water originating from the molten-salt synthesis medium.[72,74,76,77] In addition, a weak absorption between 2170 and 2200 cm^{-1} is detected which can be assigned to terminal N=C–N defects and indicates partial fragmentation and reorganisation of the CN framework under salt-mediated polymerisation conditions.[75]

The ^{13}C CP/MAS solid-state NMR spectra (Fig. 2f) confirm the structural differences indicated by ATR-FTIR. The spectrum of bCN shows two dominant resonances at 158 and 165 ppm, which are characteristic for heptazine-based CN. The signal at 158 ppm is assigned to carbon atoms in $C–N_3$ environments within tri-s-triazine units and the resonance at 165 ppm originates from carbon atoms adjacent to terminal –NH or $–NH_2$ groups at incomplete condensation sites.[78–80] A weak shoulder at approximately 163 ppm indicates minor variation in the local heptazine linkage environment, which is typically associated with hydrogen bonding or partial defects.[74,78]

In contrast, tbCN displays a broadened and downfield-shifted main resonance cantered at 163 ppm together with two weaker signals at 158 and 170 ppm. This pattern is consistent with a triazinic $C–N_3$ backbone containing residual –NH linkages and electron-deficient C=N defect sites.[78] Importantly, no signal is detected in the chemical shift region typical for nitrile carbon atoms

(110 – 125 ppm), suggesting that the IR band observed between 2170 and 2200 cm^{-1} are rather originated in defect-associated terminal N=C–N units[75] than –C≡N groups.[81] The spectral broadening of tbCN further indicates electronic heterogeneity within the framework, which is consistent with partial Li–N coordination resulting from the molten-salt synthesis.[70,72]

The presence of 1.15 wt.% residual lithium within the framework of tbCN is confirmed by ICP-OES. Thermogravimetric analysis (TGA, Fig. S6) supports this finding by revealing a non-volatile inorganic residue of 4.8 wt.% after exposure to 1000 °C under air, i.e. Li-containing species are most likely not completely removed during post-synthesis washing. In addition, tbCN shows a more pronounced mass loss below 200 °C when compared to the heptazine-based CN materials, which is attributed to the enhanced uptake of physically adsorbed and coordinated water. This behaviour is in agreement with the broad O–H feature observed in the ATR-FTIR spectrum and indicates a more hydrophilic surface compared to heptazine-CN.

The structural state of the residual lithium in tbCN was further examined by powder XRD (Fig. 2b, g). As no residual crystalline phase from the salt melt was detected (Fig. S7), a structural incorporation of Li into the CN framework is highly likely, probably through coordination to nitrogen sites or interlayer integration.[75] The diffraction pattern exhibits multiple distinct reflections in the range 10 – 35°, which are not observed for heptazine-based CN.[81–84] The absence of the characteristic (100) heptazine reflection at 13° together with the emergence of additional in-plane signals indicates a reorganisation of the framework towards triazine-based structure. At the same time the diffuse feature around 26° reflects turbostratic disorder[85] and limited interlayer coherence which is characteristic of ion-modified layered CN structures obtained via molten salt condensation.[83,84]

In contrast, bCN, spCN, saCN, and hpCN retain the two characteristic reflections commonly assigned to heptazine-based CN, namely the in-plane (100) at 13° and the (002) stacking reflection at 27°.[32,75,79,86] Variations in peak width and intensity correlate with morphological

variation rather than changes in the primary condensation structure.[23,87–89] For instance, bCN features relatively sharp stacking reflections representative of densely packed layers, while spCN and saCN exhibit broadened features due to lamellar and hierarchical nanosheets. Lastly, hpCN displays further attenuation as a result of soft-templated mesostructuring. This trend is consistent with the classical Debye–Scherrer analysis[90,91] of the crystallite thickness (Fig. S8, Tab. S1) and corresponding layer number, revealing that bCN provides an average of approx. 27 layers, saCN and spCN of 13 – 14 layers, and hpCN of only 8 layers.

To determine whether the observed differences originate solely from variations in long-range structural order, such as layer stacking and domain organisation, or also involve changes in the local bonding environment within the heptazine framework, three representative CN materials were selected for detailed comparison. bCN, spCN, and saCN cover the full range of morphological features and are not affected by impurities from salt melt (tbCN) or the potential presence of residual surfactant species (hpCN). Synchrotron-based N K-edge soft X-ray absorption spectroscopy (sXAS) spectra of bCN, spCN and saCN (Fig. 3a) exhibit nearly identical features, confirming that all three materials share the same heptazine-based coordination environment.[92] A pronounced resonance at 399 eV corresponds to π* transitions of N=C–N units within the heptazine rings, while a second feature at around 401 eV is attributed to aminic nitrogen species.[93,94] Broader absorption above 403 eV originates from σ* transitions of C–N bonds. The overall spectra and energy positions remain largely unchanged, demonstrating that variations in morphology and porosity do not affect the molecular building units of the heptazine framework.[92,93] The slightly more pronounced π*-resonances observed for bCN suggest a higher structural order or lower defect density compared to spCN and saCN.[93]

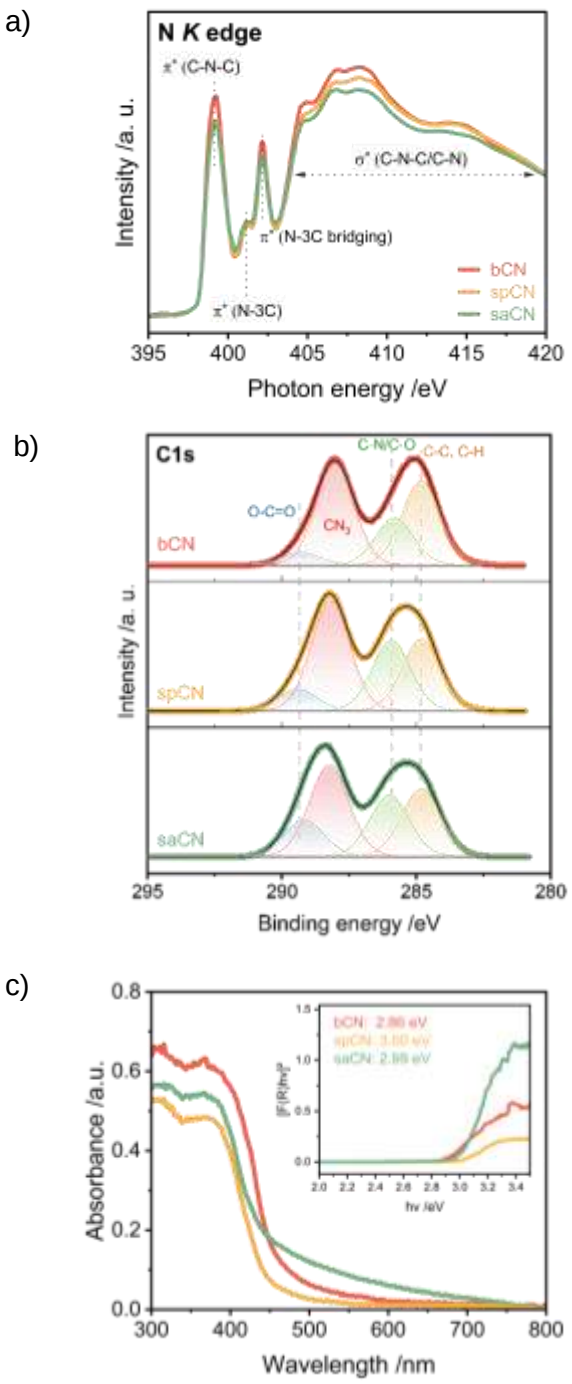

Fig. 3 Comparison of the structural and optical properties of bCN, spCN and saCN. a) N K-edge sXAS spectra. b) C 1s XPS spectra with peak deconvolutions (fitted data: black lines). c) DRS UV-vis absorption spectra with Tauc plots (inset) used to determine the optical band gaps.

XPS analyses (Fig. 3b, Fig. S9) provide complementary surface-sensitive information supporting the sXAS results. The C1s and N1s spectra of bCN, spCN and saCN are characteristic for heptazine-based CN.[95] In all samples, the main C1s component at 288.1 eV corresponds to sp^2-hybridised CN_3 species within the aromatic heptazine framework.[96,97] Additional peaks at

284.9 and 285.9 eV are attributed to defective C–C/C–H bonds and C–N/C–O bonds, respectively, while a minor peak at 289.3 eV corresponds to O–C=O species. The relative intensity of the C–O/O–C=O components increases from bCN to saCN, indicating increasing levels of surface oxidation. The observed binding energies are consistent with literature values reported for polymeric CN.[96,97] The N1s spectra are dominated by the sp^2-hybridized nitrogen (C=N–C) peak at 398.3 – 398.5 eV, accompanied by components at 399.5 ($N–(C)_3$) and 400.8 eV (C–N–H).[98,99] The increasing intensity of the C–N–H signal from bCN to saCN suggests a higher fraction of terminal nitrogen species, consistent with more open and defect-rich surface structures. Such features can promote stronger metal-support interactions and modify the electronic environment at the catalyst interface, which is beneficial for application as support in thermocatalysis.

Differences among the samples are mainly reflected in their optical properties, as revealed by UV-Vis diffuse reflectance spectroscopy (DRS UV-vis). All materials display the characteristic absorption edge of polymeric CN in the visible region (Fig. 3c) as absorption is observed for wavelengths exceeding 420 nm.[48,97] Here, bCN shows the most intense absorption in the visible range, which is in line with the densely stacked structure, while spCN exhibits a slightly red-shifted edge with lower overall intensity. Strong absorption at shorter wavelengths was observed for saCN. Tauc analysis yields optical band gaps of 2.9 eV for bCN and 3.0 eV for spCN as well as saCN. Although all three materials retain the heptazine backbone, the electronic structure varies systematically with morphology.[100] The observed changes in absorption and band gap reflect differences in conjugation length, defect concentration and nanosheet stacking. In a thermocatalytic context, these optical and electronic variations are expected to influence the interaction between the CN support and cobalt nanoparticles. The narrower band gap of bCN corresponds to stronger electronic delocalisation, which can facilitate charge redistribution at the Co–CN interface. In contrast, the wider band gap of saCN indicates reduced conjugation and a more insulating character, which may weaken electronic coupling with the supported metal. spCN represents a balanced mixture of properties of the other two materials and combines moderately

extended conjugation with increased accessible surface area. Consequently, the different CN morphologies provide distinct electronic environments that are expected to affect cobalt dispersion, redox behaviour and CO_2 activation during methanation.

3.1.2 Strategies for Modification of Al_2O_3 with bCN

Pristine CN is obtained as a fine powder with poor mechanical stability, which limits direct use in fixed-bed reactors for thermocatalytic gas phase reactions. To overcome this limitation, Al_2O_3 particles with a larger particle size were modified with CN using three different approaches (Tab. 1) targeting bCN@Al_2O_3 composites for later use as catalyst support: drop-cast (DC) of pre-synthesised bCN, co-calcination (CC) of melamine,[25,101] and Al_2O_3 and solution-deposition (SD) by impregnation of Al_2O_3 with an aqueous melamine solution followed by drying and calcination.[35,77] SEM imaging revealed a strong dependence of the quality of the modifications for the three methods (Fig. 4). The DC approach yielded discontinuous CN layers with an apparent weak adhesion to the Al_2O_3 surface. The CC resulted in the formation of large CN agglomerates, leaving extensive areas of Al_2O_3 exposed, i.e. unmodified. In contrast, the SD route yielded a uniform and conformal CN modification that provided a rather homogeneous coverage of the support surface.

Tab. 1 Overview of strategies for CN modification of Al_2O_3.

Method	Procedure	Schematic
drop-cast (DC)	bCN synthesised separately, then physically deposited via drop-casting onto Al_2O_3 and drying	
co-calcination (CC)	calcination of a physically mixture of melamine and Al_2O_3 at 550 °C	
solution-deposition (SD)	impregnation of Al_2O_3 with aqueous melamine solution, drying and calcination at 550 °C	

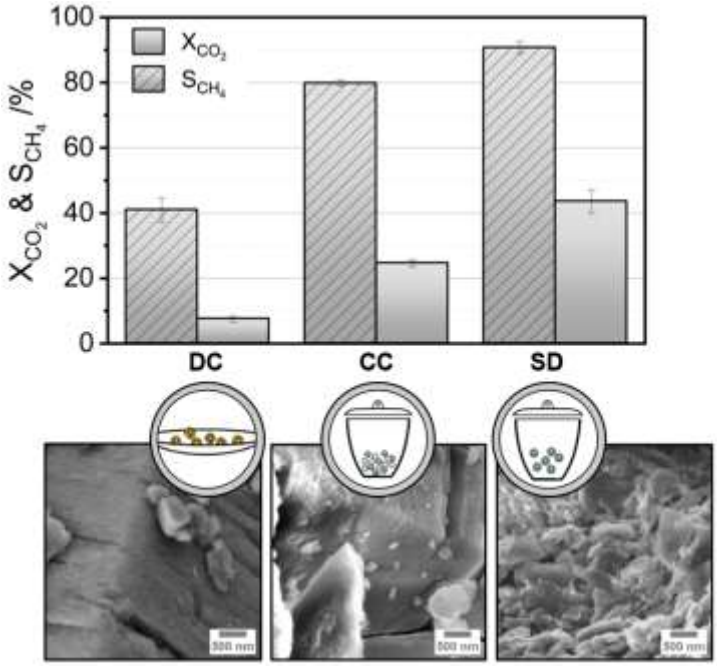

Fig. 4 Comparison of Co/bCN@Al_2O_3 catalysts during CO_2 methanation alongside schematics and representative SEM images of the modified Al_2O_3 supports. CO_2 conversion (X_{CO_2}) and CH_4 selectivity (S_{CH_4}) are shown for Co-based catalysts with CN@Al_2O_3 composites prepared by drop-casting (DC), co-calcination (CC), and solution-deposition (SD) representing average values observed during the final 5 h time on stream, while error bars indicate standard deviations. Reaction conditions: T = 325 °C, p = 5 bar_g, GHSV = 5.7 L g^{-1} h^{-1}, H_2/CO_2 = 4, CN loading w_{CN} = 29 wt.%, cobalt loading w_{Co} = 3.2 wt.%.

To directly assess the suitability of the modification strategies for effectively boosting the catalytic performance, the composites were decorated with separately synthesised Co_3O_4 nanoparticles (see Supporting Information Fig. S10 and our previous work[35] for further details on nanoparticle synthesis and characterisation) and tested in CO_2 methanation at 325 °C and 5 bar_g after *in situ* reduction of the catalysts (Fig. 4, Fig. S11, Tab. S2). A strong effect of the deposition strategy on the catalytic performance is evident despite comparable Co and CN loadings (Fig. S12). The worst performance with 8% conversion of CO_2 and a CH_4 selectivity of 41% was observed for the DC sample, which is most likely the result of insufficient modification of the Al_2O_3 by discontinuous CN layers. This is further supported as neither an activation nor a selectivity switch towards CH_4 was observed, which suggest insufficient interaction between the nanoparticles and CN.[35] The CC method enabled moderate activity (25% conversion, 80% selectivity), but incomplete CN coverage still limits the beneficial interaction between Co and CN.[35] The best performance was obtained with the SD method, reaching 43% CO_2 conversion and 91% CH_4 selectivity. These results underline that homogeneous and well-adhered CN modifications are essential for establishing consistent interactions between Co_3O_4 nanoparticles and CN-modified Al_2O_3 surfaces, which facilitates activity boost and selectivity switch during CO_2 methanation.

3.1.3 CN@Al_2O_3 Composite Supports

Based on the optimised SD method, all CN morphologies were synthesised directly on Al_2O_3 by mixing the respective precursors, drying, and subsequent polymerisation at 550 °C. In this approach, Al_2O_3 acts as a structural template that promotes the controlled formation of CN layers during thermal condensation. The resulting CN@Al_2O_3 composites are expected to exhibit distinct structural and textural properties similar to the pristine carbon nitrides. In the following, the structural and morphological properties of the CN@Al_2O_3 composites are analysed in detail to assess preservation of the morphology and identify potential alteration due to the synthesis on Al_2O_3.

TGA (Fig. S13) confirms a CN loading of 27 – 31 wt.% for all CN@Al_2O_3 composites and demonstrates thermal stability up to 400 °C, which is consistent with strong interfacial anchoring of the CN phase. SEM micrographs, N_2 physisorption, and XRD analyses confirm that also the morphology of the resulting CN@Al_2O_3 composites is determined by the CN synthesis route. However, the characteristic features of the pristine CN samples are only partially reflected by the composites. The resulting layer architecture varies considerably depending on the openness and structural nature of the respective CN type. The bCN@Al_2O_3 and spCN@Al_2O_3 composites form compact surface layers that evenly cover the majority of the external surface of Al_2O_3 (Fig. 5 and Fig. S14). This results in a significantly lower BET surface area and pore volume when compared to the bare Al_2O_3 (Fig. 5g). The N_2 adsorption isotherms show a reduced total adsorption capacity and capillary condensation at higher relative pressures (Fig. S15), confirming a narrowing of the pores when compared to pristine CN. The XRD patterns feature sharp and intense CN (002) reflections (Fig. 5h), which points towards thicker layers with increased order of crystalline domains. Overall, these observations suggest that polymerisation on Al_2O_3 proceeds via continuous film growth, resulting in closed and less permeable CN layers with limited gas accessibility.[102]

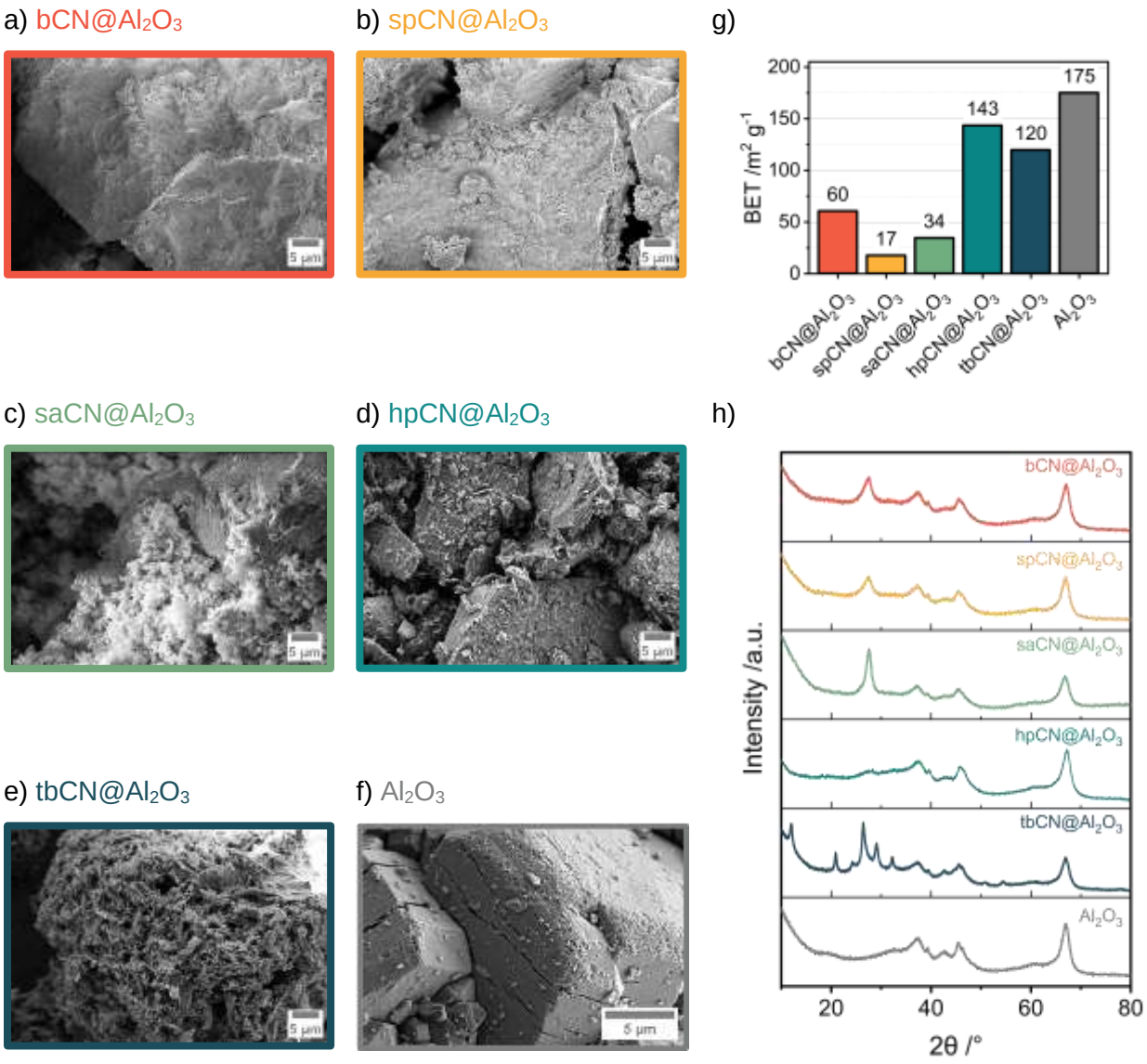

Fig. 5 Structural characterisation of the composites and bare Al_2O_3: a – f) SEM images, g) BET surface areas and h) XRD patterns.

The SEM micrographs clearly reveal differences between hpCN (Fig. 1d) and hpCN@Al_2O_3 (Fig. 5d). The hollow and highly porous network structure of hpCN is not preserved in the composite, which has an increased compactness and platelet-like structure. This suggests that the CN layer grows conformally and densely on the Al_2O_3 template, which partially covers the previously identified pores in hpCN. Nevertheless, the underlying mesoporous framework of the Al_2O_3 structure remains largely accessible, which is confirmed by the N_2 physisorption suggesting a lowered specific surface area and smaller pore volume. The broadened and less intense CN (002)

reflection for hpCN@Al_2O_3 in XRD (Fig. 5h) indicates smaller and/or less ordered graphitic domains.[83] In general, the open architecture may promote efficient gas diffusion while providing a large interface area that is advantageous for subsequent decoration with nanoparticles and catalytic application.

When compared to the largely amorphous pristine tbCN, the tbCN@Al_2O_3 composite displays a more crystalline morphology with well-defined columnar, PTI-like structures (Fig. 5) reminiscent of the architectures described in the literature.[75,103] Vertically aligned or columnar features distributed across the Al_2O_3 surface are identified in the SEM images of tbCN@Al_2O_3, suggesting that the template promotes directed nucleation and anisotropic CN growth. The composite retains a high specific surface area (120 $m^2\ g^{-1}$) and an accessible mesoporous network. This suggests that the CN modification remains porous, while the intrinsic textural properties of the tbCN and the Al_2O_3 framework both contribute to the overall accessible surface area. XRD analysis of tbCN@Al_2O_3 reveals multiple well-defined reflections between 10° and 35°, clearly distinguishable from the pattern of bare Al_2O_3. These peaks match PTI, indicating that condensation on the Al_2O_3 template induces a structural reorganisation of the triazine-based CN framework. The narrowing of the (002) reflection at 27° further points to enhanced stacking coherence and crystallinity when compared to the turbostratic tbCN precursor.[81,84] The pronounced PTI-type reflections suggest that the CN phase forms a nanocrystalline, relatively thick layer rather than a thin, amorphous layer.[81] This finding is consistent with the SEM observations of densely packed, columnar CN domains covering the Al_2O_3 surface, confirming substrate-directed condensation and structural ordering of the CN network.[70,82] The saCN@Al_2O_3 composite shows signs for both compact and open morphology, while the morphology of pristine saCN is no longer observed. Instead, fragmented, lamellar aggregates are spread irregularly across the support surface (Fig. 5c). The condensation results in partial coverage instead of the formation of spherical particles. The specific surface area of the composite decreases significantly from 77 to 34 $m^2\ g^{-1}$ and the pore size distribution reveals a smaller mesopore volume, suggesting partial pore blockage. A broadening of the CN reflections

with asymmetric shape in XRD resembles a lower stacking order and increased structural heterogeneity caused by this rearrangement.

In summary, the preservation of the pristine CN morphology after condensation on Al_2O_3 is only partially obtained and varies strongly for the studied syntheses. CN with a compact morphology, such as bCN and spCN, result in a relatively thick, mostly complete coverage of Al_2O_3 with partial blockage of pores by CN, whereas open, hierarchically structured types like hpCN and tbCN yield thin, conformal and permeable layers. The tbCN@Al_2O_3 composite develops a PTI-like columnar architecture that combines structural stability[80] with high textural openness, maintaining the mesoporosity of the support. Lastly, saCN represents an intermediate case, where partial fragmentation of the spherical organisation leads to a heterogeneous modification with moderate pore accessibility.

3.2 Catalytic Performance of CN-Modified Co-based Catalysts

For CO_2 methanation, CN@Al_2O_3 composites and bare Al_2O_3 were decorated with pre-synthesised 9 nm Co_3O_4 nanoparticles (Fig. S10).[35] By using identical loadings of the active phase (3.2 wt.% Co), the observed differences in performance can be attributed to the microstructure, quality of the modification, and surface properties of the CN layer. Methanation of CO_2 using cobalt-based catalysts represents an appealing model reaction due to the competing formation of CO, while the activity strongly depends on the cobaltous phase formed under reaction conditions. After *in situ* activation, testing was conducted at 325 °C and 5 bar_g with a H_2/CO_2 feed ratio of 4/1. The catalytic performance (Fig. S16) together with structural analysis (XRD: Fig. S19, SEM: Fig. 7) exemplify the role of the morphology and properties of the CN modification as decisive factor with respect to activity, selectivity, and stability. In addition, rate-normalised metrics, namely the CO_2 consumption rate (r_{CO_2}) and the methane space–time yield (STY_{CH_4}), were evaluated from the steady-state region of the catalytic tests (Fig. 6a). The results confirm a consistent activity order within the catalyst series, with Co/spCN@Al_2O_3 exhibiting the highest reaction rate, followed by

Co/bCN@Al_2O_3 and Co/hpCN@Al_2O_3, while the unmodified Co/Al_2O_3 catalyst shows significantly lower activity. In contrast, Co/saCN@Al_2O_3 and Co/tbCN@Al_2O_3 display only very low reaction rates under the investigated conditions. Importantly, the observed activity trends are consistent with the conversion and selectivity data (Fig. 6b), suggesting that the performance differences are intrinsic to the catalyst system and not dominated by transport or accessibility effects.

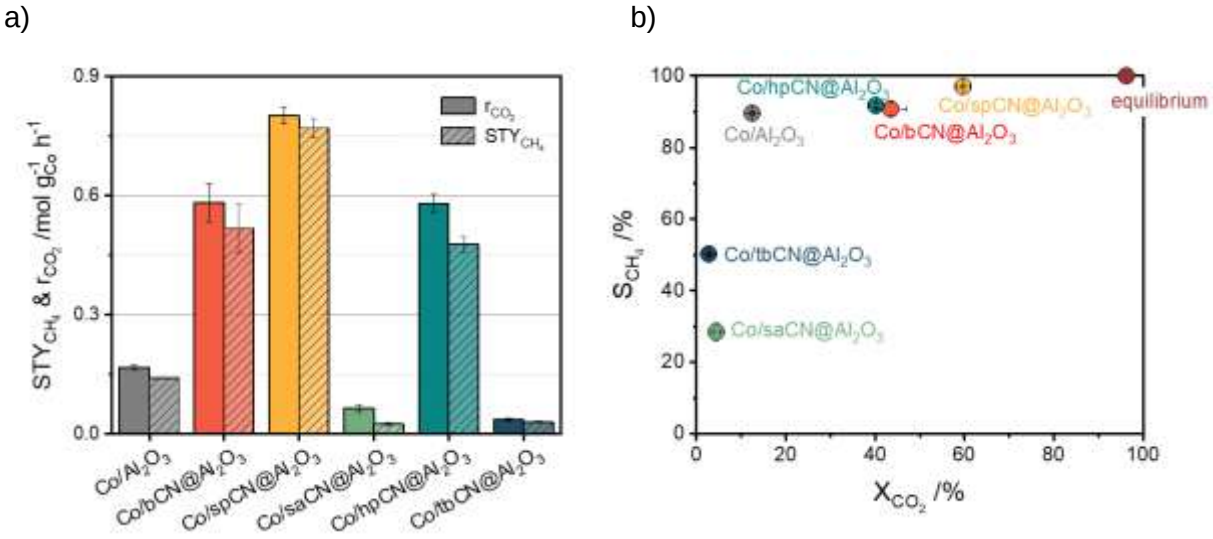

Fig. 6 Catalytic performance of Co/CN@Al_2O_3 catalysts and a Co/Al_2O_3 benchmark. a) CH_4 space–time yield (STY_{CH_4}) and CO_2 consumption rate (r_{CO_2}). b) Conversion of CO_2 (X_{CO_2}) and selectivity towards CH_4 (S_{CH_4}). The values are averaged over the final 5 h time on stream, while error bars indicate standard deviations. Reaction conditions: T = 325 °C, p = 5 bar_g, GHSV = 5.7 L g^{-1} h^{-1}, H_2/CO_2 = 4, CN loading w_{CN} = 30 wt.%, cobalt loading w_{Co} = 3.2 wt.%.

For the comparison of the performance of CN-modified catalysts during CO_2 methanation (Fig. 6), Co/bCN@Al_2O_3 serves as a starting point. As previously described,[35] the CN modification undergoes partial decomposition under reduction and reaction conditions, which promotes (surface) carburisation of cobalt and further modification by the Co–C–N interface. These structural changes were accompanied by a boost in activity and selectivity towards CH_4 during an activation period, which is also observed for the same modification, namely bCN, as well as for spCN and hpCN in the present study (Fig. S16) confirming the beneficial dynamic transformation of the catalyst during methanation. However, modification of the catalyst with saCN and tbCN did not result in this behaviour and in fact are detrimental for both activity and selectivity of the catalyst, which highlights the importance of the morphology and surface properties of the CN modification.

Expectedly, a moderate conversion level of approx. 12% with no activation period was observed for the Co/Al_2O_3 benchmark (Fig. S16). The selectivity towards CH_4 stabilised at 90%, while the activity remained relatively constant, which points towards a stable catalytic system with low intrinsic activity. CO is the only relevant carbon-containing by-product for all catalysts (Fig. S17, Tab. S4). Higher hydrocarbons were only detected in trace amounts (C_2–C_4 < 1 %), while the carbon balance (Fig. S18) was typically in the range of 95-105 % during the time interval used for activity evaluation (TOS: 4–9 h). Hence, additional carbon-containing products are not expected to form in significant quantity.

$Co/bCN@Al_2O_3$ displays a pronounced activation period during the initial 1.5 h time on stream (Fig. S16) before reaching a steady-state (CO_2 conversion: 44%; CH_4 selectivity: 91%). XRD (Fig. S19) analysis confirms the transformation of CN as the (002) stacking reflection at 27° is absent alongside a broad feature at 21° indicate partial CN degradation and formation of amorphous carbon.[104–106] In stark contrast, the triazine CN in $Co/tbCN@Al_2O_3$ remains structurally intact (Fig. S19) and fails to activate cobalt (Fig. 6). This comparison highlights that a controlled CN decomposition during activation or catalysis is preferred over mere structural stability.

Among the heptazine-based CN modifications, $Co/spCN@Al_2O_3$ displays the best performance with 60% conversion of CO_2 and a selectivity towards CH_4 of 97%. Here, the activation profile is even more pronounced (Fig. S16) due to an initially low CO_2 conversion of approx. 10%. The sponge-like morphology provides strong potential for Co–CN interaction due to the high surface area in combination with structural integrity, which enables rapid activation and excellent stability throughout the reaction. Analysis of the spent catalyst by means of SEM (Fig. 7) and XRD (Fig. S19b) confirms the presence of a residual modification maintaining a dispersed Co phase, while significant sintering cannot be identified. Aforementioned spectroscopic characterisation (UV-vis DRS, XPS and sXAS) suggests that spCN offers the most favourable balance of electronic coupling and nitrogen coordination, which is most likely linked to its superior effect on activity and stability during CO_2 methanation when used as modification of Co-based catalysts.

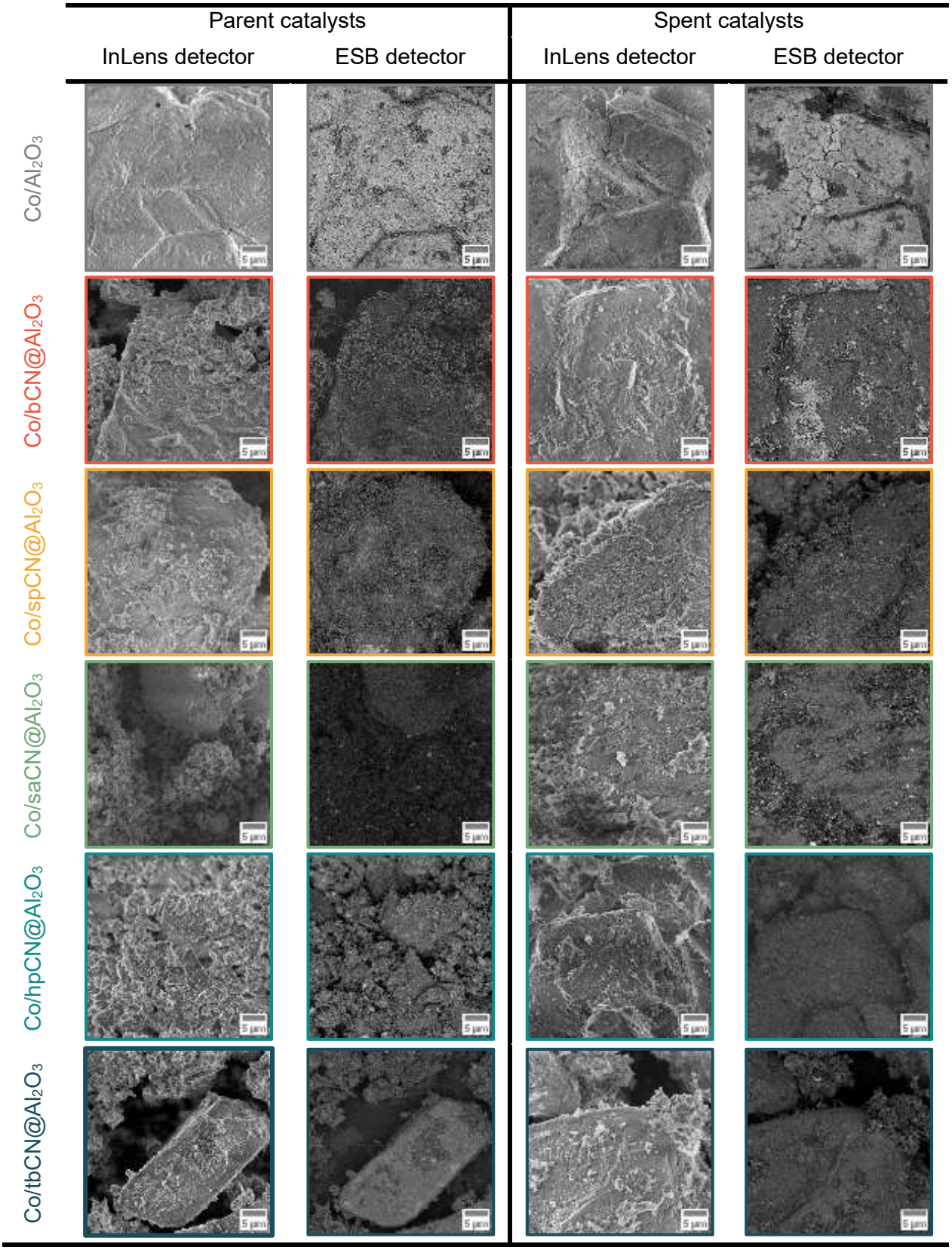

Fig. 7 SEM images of Co/CN@Al_2O_3 catalysts before (parent) and after (spent) CO_2 methanation, recorded using InLens and ESB detectors.

The catalyst employing hpCN exhibits a similar activation profile, while providing a higher initial activity upon reduction. Co/hpCN@Al_2O_3 reaches a CO_2 conversion of 40% and a CH_4 selectivity of 92% with a shorter activation period <1 h. The morphology of hpCN with wide open pores is expected to facilitate an efficient gas-solid contact and a high accessibility of cobaltous phases. SEM (Fig. 7) and XRD (Fig. S19) analyses suggest the absence of significant sintering or morphological changes, indicating that the porous CN modification effectively stabilises the metal phase. As with the other heptazine-based catalysts, the CN phase is no longer detectable after reaction due to decomposition into a carbon-rich layer that remains electronically coupled to Co. This combination of structural stability and moderate CN reactivity provides sustained activity and excellent stability under methanation conditions.

When compared to Co/Al_2O_3, the modification of the support with saCN is clearly detrimental to both conversion of CO_2 and selectivity. While the CN modification enables a high dispersion of the Co_3O_4 nanoparticles, it fails to establish a beneficial interaction with the active phase. SEM images of the parent catalyst reveal a lamellar CN that provides uniform but relatively dense surface coverage of the Al_2O_3 substrate (Fig. 7). Based on the analysis using the ESB detector, the nanoparticles appear well distributed and remain finely dispersed after reaction. However, the saCN modification partially collapses during reduction and/or methanation, which results in smoother and fused surface domains. The XRD pattern of the parent catalyst features characteristic Co_3O_4 reflections and the CN (002) stacking peak at 27° (Fig. S19a), while, a broad feature is evident at 21° after reaction (Fig. S19b) being indicative for partial conversion to a sponge-like carbonaceous structure.[25,106] Therefore, the poor catalytic performance of Co/saCN@Al_2O_3 can most likely be attributed to the intrinsic electronic properties of saCN. UV-vis DRS (Fig. 3c) revealed the widest band gap among all CN modifications, suggesting reduced π-conjugation and a more insulating character, which limits charge transfer across the Co–CN interface.[107,108] In addition, N K-edge sXAS and XPS analyses indicate (Fig. 3a, b) a higher fraction of terminal nitrogen species and a lower density of extended heptazine units, i.e. a weak electronic

coupling and low surface basicity.[107,109] Consequently, while the saCN modification provides a physically stabilising layer for cobalt, it remains electronically inert[107,109] and does not result in an increased hydrogenation activity.

The tbCN-based catalysts display a similarly poor performance with a slightly increased CH_4 selectivity of approx. 50% and an extremely low CO_2 conversion of 2%. Comparison of the catalyst before and after application in CO_2 methanation by means of SEM analyses suggests a stable morphology of the modification and a good dispersion of nanoparticles (Fig. 7). The reflections for triazine-based CN and fcc-Co are evident in the post-run analysis. Thus, the low activity of Co/tbCN@Al_2O_3 cannot be ascribed to deactivation processes as well but rather is linked to the chemical and electronic features of tbCN. The triazine-based CN framework is thermally robust[84] and electronically less conjugated than the heptazine analogues, which reduces charge delocalisation and limits electron transfer to cobalt.[107] While metallic Co is expected upon reduction and represents the catalytically active phase in this catalyst, the absence of carburisation eliminates the synergistic effect of CN modification. In addition, residual Li^+ and Cl^- ions from the CN synthesis may deteriorate performance[70] by poisoning.[110,111] Further, lithium may alter the local basicity and electronic environment, which can further weaken the Co-support interaction.[112,113]

In summary, catalytic testing establishes a clear structure-performance correlation. The morphology alongside electronic and surface properties of the CN modification of Al_2O_3 governs the multi-parameter optimisation of cobalt dispersion and stabilisation as well as catalyst activation including a selectivity switch towards CH_4. In particular, dense or chemically unfavourable CN (saCN, tbCN) result in insufficient electronic interaction and/or limited or absent effect of CN modification on Co resulting in a low catalytic activity and in part even poisoning. Whereas, open and more accessible CN structures provide more favourable conditions for metal-support interaction and catalyst activation. Among these, sponge-like structures (spCN and in part also hpCN) provide homogeneous distribution and a stabilisation of nanoparticles enabling strong

activation and stable catalytic performance. These findings highlight support engineering of CN as an effective strategy to tailor metal-support interactions and enhance the performance and stability of CO_2 methanation catalysts.

Based on its superior and reproducible catalytic performance (Fig. 6, Fig. S20), Co/spCN@Al_2O_3 was tested at extended time-on-stream to evaluate its long-term stability (Fig. 8). At 5 bar_g, the catalyst shows a short initial run-in phase as the CO_2 conversion decreases to a stable level of approx. 50%, which is afterwards maintained over 50 h. At elevated pressure (20 bar_g), a more pronounced initial change is observed due to the substantially harsher conditions with a drop in CO_2 conversion from 80% to 60%, followed by a stable steady-state regime that is maintained over 100 h. In both cases, the CH_4 selectivity remains consistently close to 100% throughout the entire experiment. Importantly, no indication of catalyst deactivation is observed after the initial stabilisation, even under prolonged operation at elevated pressure.

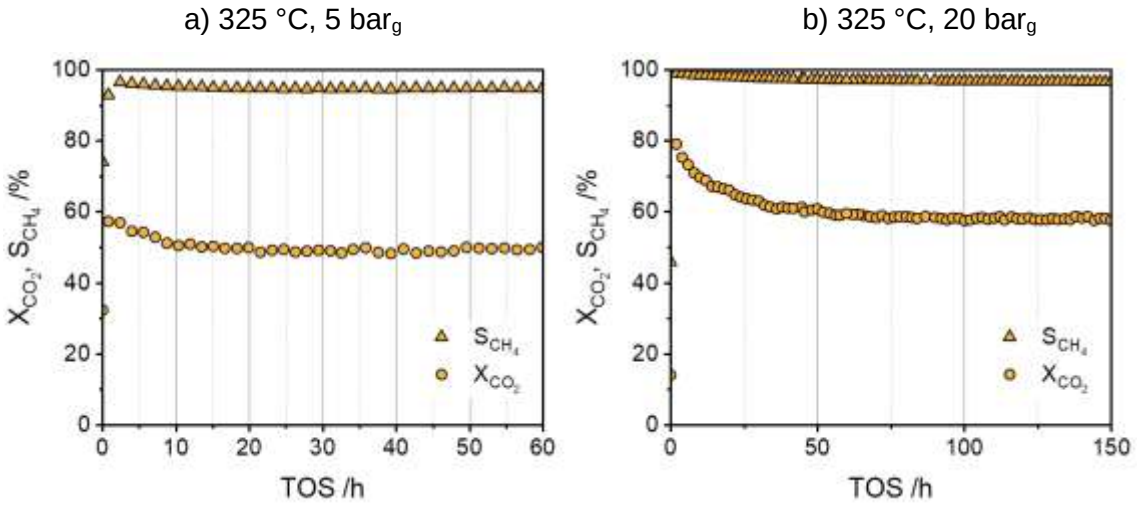

Fig. 8 Catalytic performance of Co/spCN@Al_2O_3 during CO_2 methanation (a) over an extended time-on-stream and (b) with additionally elevated pressure. CO_2 conversion (X_{CO_2}, circles) and CH_4 selectivity (S_{CH_4}, triangles) during long-time testing at 325 °C and (a) 5 bar_g (60 h) and (b) 20 bar_g (150 h). Reaction conditions: GHSV = 5.7 L g^{-1} h^{-1}, H_2/CO_2 = 4, w_{Co} = 3.2 wt.%.

To clarify the nature of the CN-derived phase formed during reaction, the spent Co/spCN@Al_2O_3 catalyst from the 9 h experiments (Fig. 6, Fig. S20) was analysed in detail. XRD analysis of Co/spCN@Al_2O_3_spent (Fig. S19) displays that the initial CN structure is no longer preserved. Instead, a broad feature at lower diffraction angles appears, which can be assigned to disordered

or amorphous carbon phases. Such transformations have been reported for CN-based materials, where the original CN framework collapses and metal-assisted restructuring leads to graphitic or turbostratic carbon with altered interlayer spacing and reduced structural order.[24,106]

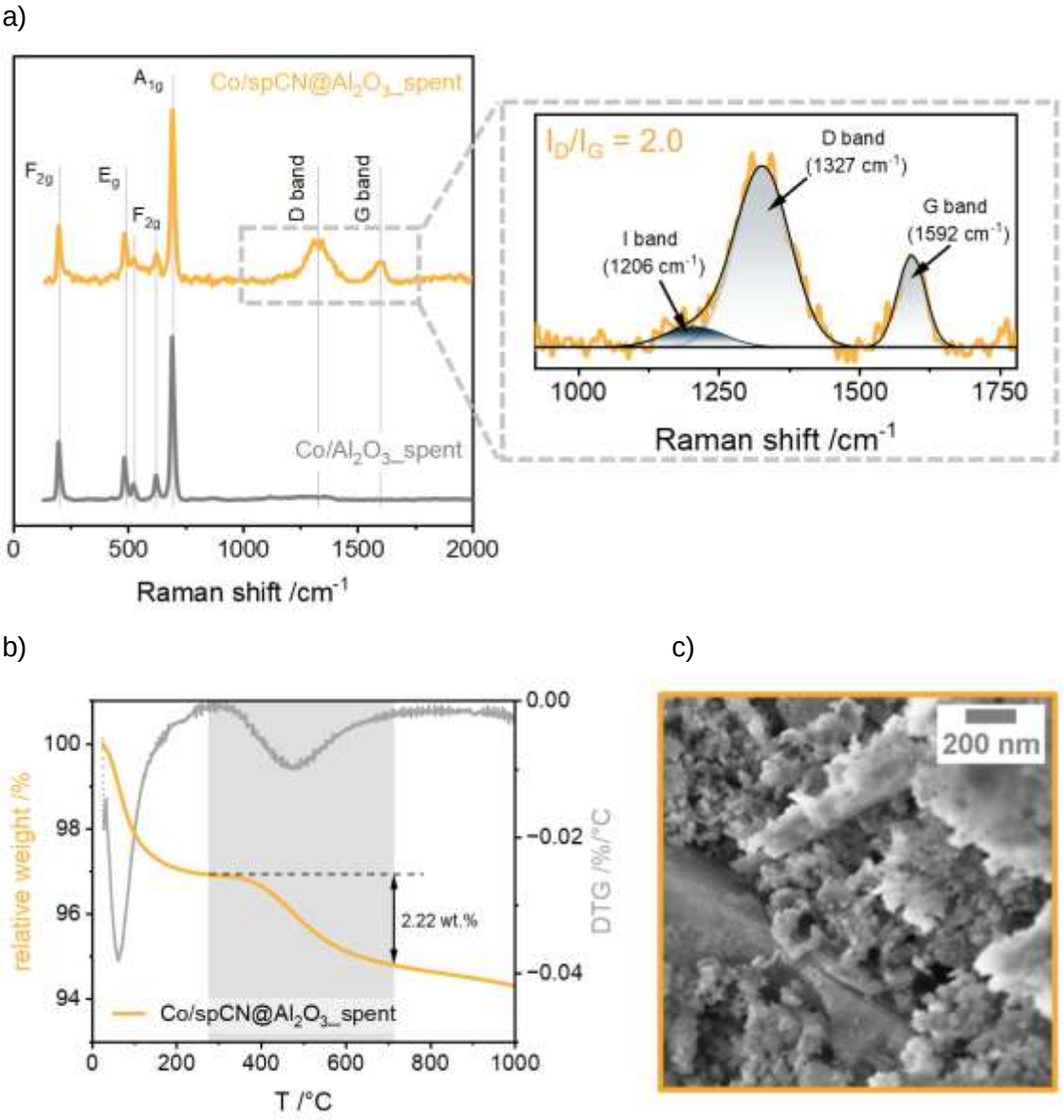

Fig. 9 Physicochemical characterisation of the spent catalyst. a) Raman spectra of Co/spCN@Al_2O_3_spent (orange) and Co/Al_2O_3_spent (grey). b) TGA of Co/spCN@Al_2O_3_spent. c) SEM image Co/spCN@Al_2O_3_spent.

Raman spectroscopy of Co/spCN@Al_2O_3_spent (Fig. 9a) further supports this interpretation. The spectrum reveals clear structural changes when compared to Co/Al_2O_3. While the latter does not exhibit any significant Raman features in the region characteristic for carbon materials, the CN-

modified catalyst shows two pronounced bands at 1350 and 1580 cm^{-1}, which can be assigned to the D and G bands of sp^2-hybridised carbon, respectively.[114–116]

In addition, bands attributed to Co_3O_4 (F_{2g}, E_g, $A1_g$ modes) are identified at low inverse wavenumbers, i.e. passivated cobalt oxide species.[117] The relatively high intensity of the D band ($I_D/I_G \approx 2.0$) indicates a high density of structural defects and a limited lateral extension of ordered sp^2 domains. The D band is associated with breathing modes of sp^2 carbon rings with A_{1g} symmetry and becomes Raman-active in the presence of structural disorder, whereas the G mode has E_{2g} symmetry and corresponds to the in-plane stretching vibration of sp^2 carbon networks.[115,118–120] In particular, the D band exhibits a pronounced asymmetry with a distinct shoulder to lower inverse wavenumbers. While the defect-activated nature of the D band implies that its spectral shape is governed by a distribution of resonance processes, including contributions associated with Stokes and anti-Stokes scattering, these are expected to result in a continuous broadening rather than the formation of a clearly resolvable sub-feature.[115] The presence of a defined shoulder cannot be fully rationalised by the superposition of resonance-induced contributions alone. Instead, this feature indicates an additional vibrational contribution at 1206 cm^{-1}. Maldonado *et al.*[121] reported a comparable feature in this region for nitrogen-doped carbon materials and assigned it to the so-called I-band. This band has been attributed to a relaxation of symmetry within the sp^2 carbon lattice, where structural distortions associated with the coexistence of sp^2 and sp^3-hybridised carbon environments activate otherwise Raman-inactive phonon modes of the density of states.[106,118]

Further support is provided by Pietrowski *et al*.,[106] who reported a similar band at 1178 cm^{-1} in N-doped carbon nanotubes derived from CN and assigned it to the I-band, which is characteristic of nitrogen incorporated into the carbon framework. Notably, these nanotube structures arise from the transformation of CN during thermal treatment or catalytic applications. Accordingly, it is well established that CN may reorganise into amorphous carbon structures,[24,25,35] including N-doped graphitic domains or nanotube-like morphologies.[106,122] The additional band at 1206 cm^{-1} therefore

indicates that the carbonaceous phase formed in Co/spCN@Al_2O_3 under reaction conditions is not only highly defective, but still contains nitrogen incorporated within the sp^2 carbon network. This is consistent with the high I_D/I_G ratio of ~2, which matches values reported by Pietrowski *et al*.[106] and Sharifi *et al.*[123] for N-doped carbon materials containing around 5% nitrogen.

TGA of the spent catalyst shows only a small mass loss attributable to oxidisable carbon species (Fig. 9b). The catalyst contains a substantial fraction of inert components, including Al_2O_3 as well as residual SiC and quartz wool from the reactor packing, which render an exact analysis of the carbon content by TGA challenging. SEM analysis provides complementary morphological evidence (Fig. 9c). The catalyst surface remains covered by a continuous, layer-like structure even after reaction. The persistence of these surface layers indicates that a carbonaceous phase remains associated with the support. This observation is consistent with reports describing the transformation of CN into sponge-like or fibrous carbon structures that retain surface coverage despite structural reorganisation.

Finally, the previously observed correlation between modification quality and catalytic performance (Fig. 4) was confirmed for Co/spCN@Al_2O_3 as superior catalyst (Fig. S22, Tab. S5). Similar to the Co/bCN@Al_2O_3, the catalytic performance strongly depends on the method with SD resulting in the best performance.

3.3 *operando* DRIFTS Evidence for Interfacial Synergy

To investigate the role of the Al_2O_3-CN interface on the observed performance boost by CN modification of the support, a Co/spCN catalyst without Al_2O_3 was prepared and compared to Co/spCN@Al_2O_3 in *operando* studies (Fig. S23). Temperature-resolved DRIFTS was conducted in the range of 100 – 400 °C within the wavenumber region of 2100 – 1150 cm^{-1} to study adsorption of species containing carbon oxide bonds. The spectra were acquired after the temperature reached steady state. The spectra reveal the presence of various surface-bound intermediates on Co/spCN@Al_2O_3 (Fig. 10), which are not detected for the catalyst without Al_2O_3, i.e. the CN-Al_2O_3

interface enables active contribution of the composite to the catalytic process (Tab. 2). At low temperatures between 100 and 300 °C, the formation of bicarbonates is detected at 1647, 1442 and 1228 cm^{-1}.[124–126] After maximum absorbance at 100 °C, a decreasing concentration is observed when increasing temperature to 300 °C, while formate peaks are detected at 1593, 1393 and 1373 cm^{-1} at temperatures exceeding 200 °C.[124,127] As bicarbonate is formed by the adsorption of CO_2 on the hydroxy groups of the Al_2O_3 support and elevated temperatures result in the conversion to formate, a supply of activated hydrogen must be enabled. Hence, the reaction from bicarbonate to formate most likely takes place at the interface between the phases Co, CN, and Al_2O_3. Hydrogen is activated on Co, whereby activated H atoms can move freely to the Al_2O_3 support.[124] Two distinct peaks are observed in the temperature-resolved spectra for the wavenumber range between 4000 and 1150 cm^{-1} at 2360 and 2343 cm^{-1} (Fig. S24), which can be assigned to CO_2 in the gas phase.[124,125] The peaks from CO_2 decrease with increasing temperature since the absorption of infrared light depend on the temperature. From 250 °C onwards, the decrease in the signal strength of CO_2 is enhanced since CO_2 is converted to CH_4. This is followed by a peak at 3014 cm^{-1}, which can be assigned to the CH groups of the CH_4 molecule and is further enhanced when increasing the temperature up to 400 °C.[124,127]

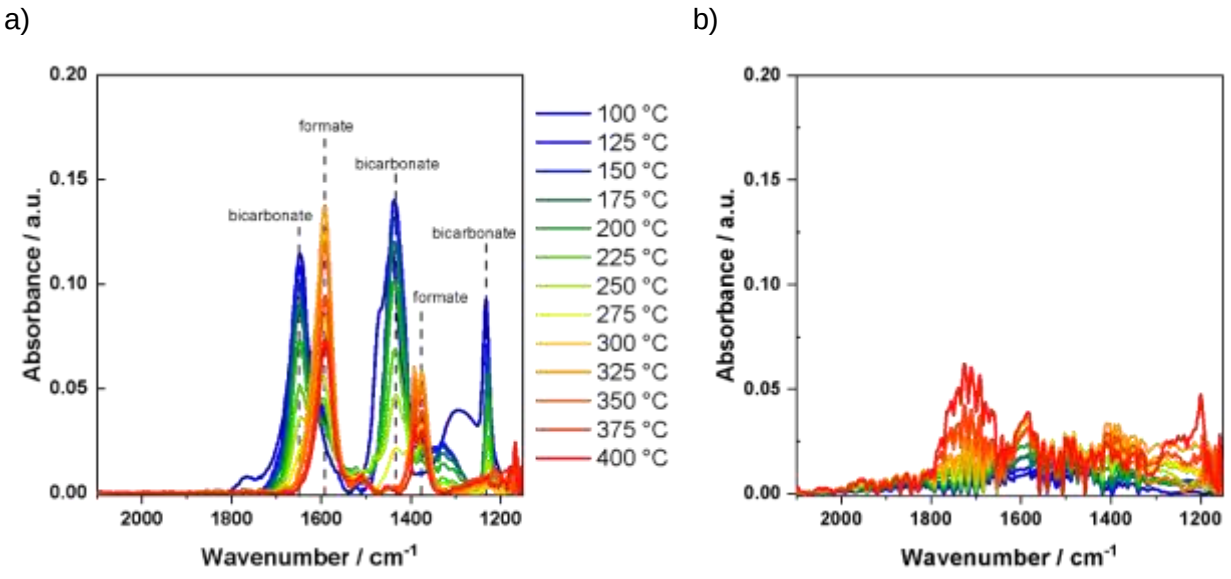

Fig. 10 Temperature-resolved DRIFTS using a) Co/spCN@Al_2O_3 and b) Co/spCN during CO_2 methanation at 5 bar_g using a $CO_2/H_2/N_2$ feed gas composition of 1/4/5 and a GHSV of 276 L g^{-1} h^{-1}.

Different species are identified in the temperature-resolved spectra of the Co/spCN catalyst (Fig. 10b). From 2000 to 1300 cm^{-1}, several peaks can be assigned to the absorption of OH groups. The absence of other adsorbed species reveals that the CN phase alone does not significantly add adsorption sites for CO_2. In the temperature-resolved spectra (Fig. S25) in the range from 4000 – 1150 cm^{-1}, the CO_2 peaks are, once again, detectable in addition to CO in the gas phase at 2130 cm^{-1}.

Tab. 2 Adsorbates and their respective Absorption at different wavenumbers for the CO_2 methanation.

Adsorbate	Wavenumber / cm^{-1}	
bicarbonate	1228, 1442, 1647	124–126
formate	1373, 1393, 1593, 2900	124,127
CH_4	1305, 3014	124,127
CO_2	2343, 2360	124,125
CO	2130	125

The enhanced activity of the Co/spCN@Al_2O_3 catalyst when compared to Co/Al_2O_3 can therefore be attributed to a strong synergistic interaction between the CN and the Al_2O_3 aside from beneficial effects on the active Co phase. Such heterointerfaces between basic and acidic components are known to profoundly influence the electronic and structural properties of catalysts.[128] Al_2O_3 acts as a Lewis-acidic oxide, while CN provides Lewis-basic nitrogen sites capable of coordinating to surface Al^{3+} centres. The resulting acid-base interaction forms a stable CN@Al_2O_3 interface accompanied by charge redistribution and defect generation within the CN modification.

Previous studies have shown that CN/Al_2O_3 heterojunctions promote interfacial electron transfer and polarisation, thereby increasing the electron density on the CN surface and enhancing catalytic reactivity.[48,129] These interfacial effects also influence the redox behaviour of Co_3O_4 nanoparticles supported on CN@Al_2O_3. Liu *et al.*[130] showed that CN can tune the Co 3d states, facilitating the Co^{3+}/Co^{2+} redox cycle and improving oxygen activation kinetics.[128] Similarly, nanoparticle-support interactions in Co_3O_4/Al_2O_3 systems determine the redox properties of surface oxygen species and thus the overall catalytic activity.[131] Therefore, introduction of a CN

interlayer between Co_3O_4 and Al_2O_3 creates a triple interface (Co–CN–Al_2O_3) that combines electronic tuning with structural stabilisation.[25] The CN shell further anchors Co_3O_4 nanoparticles via Co–N coordination, which may suppress sintering and facilitate electronical enrichment. It has also been shown that such Co–N bonding facilitates electron transfer[128] and preserves small Co domains, thereby enhancing catalytic activity.[25,26,35,132]

Overall, the CN-Al_2O_3 interaction plays a pivotal role in tailoring the electronic environment at the catalyst interface. The combined effects of (i) interfacial charge transfer between CN and Al_2O_3, (ii) improved Co–N coordination and (iii) enhanced nanoparticle dispersion provide a collective explanation for the superior catalytic performance and stability of Co/spCN@Al_2O_3.

4. Summary and Conclusion

This study explores CN as a versatile and adaptable support modification for Co-catalysed CO_2 methanation. Further, the importance of the morphology and interaction of CN with cobalt as well as Al_2O_3 is demonstrated. Comprehensive characterisation confirms that different degrees of Al_2O_3 surface coverage are achieved when targeting various morphologies of CN, which strongly affects pore accessibility and the dispersion of Co_3O_4 nanoparticles. Further, pristine CN in part strongly differs from CN grown on Al_2O_3 during solution-deposition via impregnation of the support with CN precursors followed by calcination/polycondensation. Catalytic testing exhibits vast differences in catalytic properties during CO_2 methanation, which range from strong activation alongside a selectivity switch towards CH_4 to detrimental effects of CN modification. Among the investigated materials, spCN provides the most efficient modification for methane production achieving 60% conversion of CO_2 and a selectivity towards CH_4 of 97% at 325 °C and 5 bar_g. Contrary to heptazine-based CN, modification of Al_2O_3 with triazine-based and self-assembled CN (tbCN, saCN) was detrimental, resulting in a poor performance due to their limited electronic coupling and insufficient CN reactivity under reaction conditions.

Post-reaction analyses and *operando* DRIFTS indicate that CN introduces an additional interaction pathway between cobalt and Al_2O_3, improving charge transfer, suppresses sintering, and promoting the formation of a transient Co–C–N species under reaction conditions. The sponge-like CN morphology provides the most favourable balance of structural defects and electronic interaction, resulting in beneficial metal dispersion and stability.

Overall, these findings highlight the use of CN as a practical and highly tuneable modification strategy for tailoring support properties in thermocatalytic CO_2 hydrogenation. The results further indicate that controlling CN morphology provides a strategy for the targeted development of multifunctional composite supports in thermocatalysis, in which interfacial chemistry is deliberately adjusted to optimise catalytic performance.

Author contributions

A.B. conceptualised the study, developed the overall research strategy, and carried out the materials synthesis, catalytic testing and comprehensive characterisation, performed the data analysis and wrote the majority of the original draft of the manuscript. T.E. conceived and conducted the DRIFTS experiments, analysed and interpreted the corresponding data, and contributed to writing the manuscript. P.N. performed the sXAS measurements at the beamline and carried out the analysis and visualisation of the sXAS data. R.D. and M.R. provided supervision and resources for the DRIFTS studies and contributed to scientific discussion and interpretation of the results. M.W. contributed to the conceptualisation of the study, supervised the project, acquired funding, provided critical input to data interpretation, and substantially reviewed and edited the manuscript. All authors discussed the results, contributed to manuscript revision, and approved the final version.

Acknowledgements

The authors acknowledge financial support from the Helmholtz Research Program Materials and Technologies for the Energy Transition (MTET), Topic 3: Chemical Energy Carriers and hte GmbH – the high throughput experimentation company via the STAR budget programme. Technical support in sample characterisation is gratefully acknowledged from Asad Asadli (Raman), Dr. Michael Zimmermann (SEM), Dr. Tom Zevaco (ssNMR), Armin Lautenbach and Elisabeth Herzinger (ICP-OES), Marion Lenzner (TGA), as well as Nikolaj Aljoscha Slaby, Doreen Neumann-Walter, and Dr. Thomas Nicola Otto (N_2 physisorption). Balász Molnar is thanked for assistance with sample preparation for DRIFTS measurements. Dr. Ulrich Arnold is acknowledged for providing laboratory infrastructure for CO_2 hydrogenation experiments. The authors also thank

Dr. Bärbel Krause (Institute for Photon Science and Synchrotron Radiation, KIT) for her support during the XPS measurements.

Conflicts of interest

There are no conflicts to declare.

Data availability statement

All data is openly available on Repo4Cat (https://repository.nfdi4cat.org/) via the link: https://hdl.handle.net/21.11165/4cat/XXXX-XXXX.

References

1. Vogt, C.; Monai, M.; Kramer, G. J., et al. *Nat. Catal.* **2019**, 2 (3), 188–197. DOI: 10.1038/s41929-019-0244-4.
2. Frontera, P.; Macario, A.; Ferraro, M., et al. *Catalysts* **2017**, 7 (2), 59. DOI: 10.3390/catal7020059.
3. Usman, M.; Podila, S.; Alamoudi, M. A., et al. *Catalysts* **2025**, 15 (3), 203. DOI: 10.3390/catal15030203.
4. Ullah, S.; Yang, X.; Khan, Z. U., et al. *New J. Chem.* **2025**, 49 (17), 7097–7125. DOI: 10.1039/D5NJ01108F.
5. Lyu, S.; Zhao, D.; Zhang, H., et al. *Carbon Capture Science & Technology* **2025**, 14, 100381. DOI: 10.1016/j.ccst.2025.100381.
6. Zhou, X.; Price, G. A.; Sunley, G. J., et al. *Angew. Chem.* **2023**, 62 (52), e202314274. DOI: 10.1002/anie.202314274.
7. Fan, T.; Liu, H.; Shao, S., et al. *J. Phys. Chem. Lett.* **2021**, 12 (43), 10486–10496. DOI: 10.1021/acs.jpclett.1c03043.
8. Shen, Y.; Cao, Z.; Xiao, Z. *Catalysts* **2019**, 9 (5), 423. DOI: 10.3390/catal9050423.
9. Have, I. C. ten; Kromwijk, J. J. G.; Monai, M., et al. *Nat. Commun.* **2022**, 13 (1), 324. DOI: 10.1038/s41467-022-27981-x.
10. Wolf, M.; Mutuma, B. K.; Coville, N. J., et al. *ACS Catal.* **2018**, 8 (5), 3985–3989. DOI: 10.1021/acscatal.7b04177.
11. Wang, M.; Wang, P.; Zhang, G., et al. *Sci. Adv.* **2023**, 9 (24), eadg0167. DOI: 10.1126/sciadv.adg0167.
12. Yu, Y.; Mottaghi-Tabar, S.; Iqbal, M. W., et al. *Catal. Today* **2021**, 379, 250–261. DOI: 10.1016/j.cattod.2020.08.017.
13. Chen, Z.; Du, J.; Chen, D., et al. *Catalysts* **2025**, 15 (4), 329. DOI: 10.3390/catal15040329.
14. Luo, D.; Liu, X.; Chang, T., et al. *Phys. Chem. Chem. Phys.* **2024**, 26 (6), 5704–5712. DOI: 10.1039/D3CP06041A.
15. Tsiotsias, A. I.; Charisiou, N. D.; Yentekakis, I. V., et al. *Catalysts* **2020**, 10 (7), 812. DOI: 10.3390/catal10070812.
16. Kuhaudomlap, S.; Srifa, A.; Koo-Amornpattana, W., et al. *Sci. Rep.* **2024**, 14 (1), 23149. DOI: 10.1038/s41598-024-73848-0.
17. González-Rangulan, V. V.; Reyero, I.; Bimbela, F., et al. *Catalysts* **2023**, 13 (2), 448. DOI: 10.3390/catal13020448.
18. Khasu, M.; Marquart, W.; Kooyman, P. J., et al. *ACS Catal.* **2023**, 13 (10), 6862–6872. DOI: 10.1021/acscatal.3c00924.
19. Lee, Y. H.; Ahn, J. Y.; Nguyen, D. D., et al. *RSC Adv.* **2021**, 11 (29), 17648–17657. DOI: 10.1039/d1ra02327f.
20. Italiano, C.; Llorca, J.; Pino, L., et al. *Appl. Catal. B: Environ.* **2020**, 264, 118494. DOI: 10.1016/j.apcatb.2019.118494.
21. Bhanderi, D.; Lakhani, P.; Modi, C. K. *RSC Sustainability* **2024**, 2 (2), 265–287. DOI: 10.1039/D3SU00382E.
22. Hou, S.; Gao, X.; Lv, X., et al. *Nano-Micro Lett.* **2024**, 16 (1), 70. DOI: 10.1007/s40820-023-01297-x.

23. Wu, G.; Zhang, W.; Mo, Z., et al. *ACS Catal.* **2025**, 15 (11), 8822–8832. DOI: 10.1021/acscatal.5c01086.

24. Park, H.; Youn, D. H.; Kim, J. Y., et al. *ChemCatChem* **2015**, 7 (21), 3488–3494. DOI: 10.1002/cctc.201500794.

25. Park, H.; Kim, K. Y.; Youn, D. H., et al. *ChemCatChem* **2017**, 9 (21), 4098–4104. DOI: 10.1002/cctc.201700613.

26. Zhao, Y.; Huang, S.; Liu, C., et al. *J. Taiwan Inst. Chem. Eng.* **2024**, 156, 105328. DOI: 10.1016/j.jtice.2023.105328.

27. Oliaei Torshizi, H.; Nakhaei Pour, A.; Mohammadi, A., et al. *New J. Chem.* **2020**, 44 (15), 6053–6062. DOI: 10.1039/D0NJ01041C.

28. SUN, Y.; GAO, X.; MA, Q., et al. *J. Fuel Chem. Technol.* **2024**, 52 (1), 19–28. DOI: 10.1016/S1872-5813(23)60378-0.

29. Zhang, Y.; Guo, X.; Liu, B., et al. *Fuel* **2021**, 305, 121473. DOI: 10.1016/j.fuel.2021.121473.

30. Ahmad, K. N.; Anuar, S. A.; Wan Isahak, W. N. R., et al. *ACS Appl. Mater. Interfaces* **2020**, 12 (6), 7102–7113. DOI: 10.1021/acsami.9b18984.

31. Pieta, I. S.; Gieroba, B.; Kalisz, G., et al. *Ind. Eng. Chem. Res.* **2022**, 61 (29), 10496–10510. DOI: 10.1021/acs.iecr.2c00452.

32. Refaat, Z.; Saied, M. E.; Naga, A. O. A. E., et al. *Sci. Rep.* **2023**, 13 (1), 4855. DOI: 10.1038/s41598-023-31958-1.

33. Ahmad, K. N.; Wan Isahak, W. N. R.; Rosli, M. I., et al. *Appl. Surf. Sci.* **2022**, 571, 151321. DOI: 10.1016/j.apsusc.2021.151321.

34. Yu, Y.; Chan, Y. M.; Bian, Z., et al. *Int. J. Hydrog. Energy* **2018**, 43 (32), 15191–15204. DOI: 10.1016/j.ijhydene.2018.06.090.

35. Barthelmeß, A.; Wambo Tchatchou, A. J.; Zimmermann, M., et al. *ChemCatChem* **2025**. DOI: 10.1002/cctc.202500506.

36. Yang, T.; Mao, X.; Zhang, Y., et al. *Nat. Commun.* **2021**, 12 (1), 6022. DOI: 10.1038/s41467-021-26316-6.

37. Yang, H.; Goldbach, A.; Wei, J., et al. *ACS Catal.* **2024**, 14 (10), 7444–7455. DOI: 10.1021/acscatal.4c00995.

38. Alaghmandfard, A.; Ghandi, K. *Nanomaterials* **2022**, 12 (2), 294. DOI: 10.3390/nano12020294.

39. Acharya, R.; Parida, K. *J. Environ. Chem. Eng.* **2020**, 8 (4), 103896. DOI: 10.1016/j.jece.2020.103896.

40. Li, G.; Nie, X.; Chen, J., et al. *Water research* **2015**, 86, 17–24. DOI: 10.1016/j.watres.2015.05.053.

41. Crake, A.; Christoforidis, K. C.; Godin, R., et al. *Appl. Catal. B: Environ.* **2019**, 242, 369–378. DOI: 10.1016/j.apcatb.2018.10.023.

42. Christoforidis, K. C.; Montini, T.; Fittipaldi, M., et al. *ChemCatChem* **2019**, 11 (24), 6408–6416. DOI: 10.1002/cctc.201901703.

43. Zou, W.; Shao, Y.; Pu, Y., et al. *Appl. Catal. B: Environ.* **2017**, 218, 51–59. DOI: 10.1016/j.apcatb.2017.03.085.

44. Huang, L.; Li, Y.; Xu, H., et al. *RSC Adv.* **2013**, 3 (44), 22269. DOI: 10.1039/c3ra42712a.

45. Qiao, Q.; Yang, K.; Ma, L.-L., et al. *J. Phys. D: Appl. Phys.* **2018**, 51 (27), 275302. DOI: 10.1088/1361-6463/aac817.

46. Saman, F.; Bahruji, H.; Mahadi, H. *IOP Conf. Ser.: Earth Environ. Sci.* **2022**, 997 (1), 12018. DOI: 10.1088/1755-1315/997/1/012018.

47. Saravanan, V.; Lakshmanan, P.; Ramalingan, C. *Diam. Relat. Mater.* **2021**, 114, 108291. DOI: 10.1016/j.diamond.2021.108291.

48. Li, F.-T.; Zhao, Y.; Wang, Q., et al. *J. Hazard. Mater.* **2015**, 283, 371–381. DOI: 10.1016/j.jhazmat.2014.09.035.

49. Wang, X.-J.; Liu, C.; Li, X., et al. *Appl. Surf. Sci.* **2017**, 394, 340–350. DOI: 10.1016/j.apsusc.2016.10.081.

50. Zhang, S.; Su, C.; Ren, H., et al. *Nanomaterials* **2019**, 9 (2). DOI: 10.3390/nano9020215.

51. Lu, L.; Wang, G.; Zou, M., et al. *Appl. Surf. Sci.* **2018**, 441, 1012–1023. DOI: 10.1016/j.apsusc.2018.02.080.

52. Idrees, F.; Dillert, R.; Bahnemann, D., et al. *Catalysts* **2019**, 9 (2), 169. DOI: 10.3390/catal9020169.

53. Thomas, A.; Fischer, A.; Goettmann, F., et al. *J. Mater. Chem.* **2008**, 18 (41), 4893. DOI: 10.1039/b800274f.

54. Kharlamov, A.; Bondarenko, M.; Kharlamova, G., et al. *Diam. Relat. Mater.* **2016**, 66, 16–22. DOI: 10.1016/j.diamond.2016.03.012.

55. Jun, Y.-S.; Lee, E. Z.; Wang, X., et al. *Adv. Funct. Materials.* **2013**, 23 (29), 3661–3667. DOI: 10.1002/adfm.201203732.

56. Peer, M.; Lusardi, M.; Jensen, K. F. *Chem. Mater.* **2017**, 29 (4), 1496–1506. DOI: 10.1021/acs.chemmater.6b03570.

57. Peng, L.; Peng, Y.; Primo, A., et al. *ACS Appl. Mater. Interfaces* **2021**, 13 (11), 13499–13507. DOI: 10.1021/acsami.0c19463.

58. Basin, A. S.; Kaplun, A. B.; Meshalkin, A. B., et al. *Russ. J. Inorg. Chem.* **2008**, 53 (9), 1509–1511. DOI: 10.1134/S003602360809026X.

59. Shi, N.; Cheng, W.; Zhou, H., et al. *Chem. Commun.* **2015**, 51 (7), 1338–1340. DOI: 10.1039/c4cc08179j.

60. Wolf, M.; Fischer, N.; Claeys, M. *Mater. Chem. Phys.* **2018**, 213, 305–312. DOI: 10.1016/j.matchemphys.2018.04.021.

61. Pinna, N.; Niederberger, M. *Angew. Chem.* **2008**, 47 (29), 5292–5304. DOI: 10.1002/anie.200704541.

62. Wolf, M.; Fischer, N.; Claeys, M. *Nanoscale Adv.* **2019**, 1 (8), 2910–2923. DOI: 10.1039/c9na00291j.

63. Wolf, M.; Fischer, N.; Claeys, M. *J. Catal.* **2019**, 374, 199–207. DOI: 10.1016/j.jcat.2019.04.030.

64. Engl, T.; Langer, M.; Freund, H., et al. *Chem. Ing. Tech.* **2023**, 95 (5), 658–667. DOI: 10.1002/cite.202200204.

65. Weber, D.; Engl, T.; Raabe, M., et al. *Appl. Catal. A: Gen.* **2025**, 708, 120582. DOI: 10.1016/j.apcata.2025.120582.

66. Wolf, M.; Fischer, N.; Claeys, M. *Catal. Today* **2016**, 275, 135–140. DOI: 10.1016/j.cattod.2016.05.003.

67. Dias, Y. R.; Perez-Lopez, O. W. *J. Environ. Chem. Eng.* **2021**, 9 (1), 104629. DOI: 10.1016/j.jece.2020.104629.

68. Wang, Z.; Guan, W.; Sun, Y., et al. *Nanoscale* **2015**, 7 (6), 2471–2479. DOI: 10.1039/c4nr05732e.

69. Thommes, M.; Cychosz, K. A. *Adsorption* **2014**, 20 (2-3), 233–250. DOI: 10.1007/s10450-014-9606-z.

70. Wirnhier, E.; Döblinger, M.; Gunzelmann, D., et al. *Chem. Eur. J.* **2011**, 17 (11), 3213–3221. DOI: 10.1002/chem.201002462.

71. Zhang, B.; Wang, Q.; Zhuang, J., et al. *J. Photochem. Photobiol. A: Chem.* **2018**, 362, 1–13. DOI: 10.1016/j.jphotochem.2018.05.009.

72. Miller, T. S.; Jorge, A. B.; Suter, T. M., et al. *Phys. Chem. Chem. Phys.* **2017**, 19 (24), 15613–15638. DOI: 10.1039/c7cp02711g.

73. Zhang, Z.; Leinenweber, K.; Bauer, M., et al. *J. Am. Chem. Soc.* **2001**, 123 (32), 7788–7796. DOI: 10.1021/ja0103849.

74. Xu, C.; Liu, H.; Wang, D., et al. *Appl. Catal. B: Environ.* **2023**, 334, 122835. DOI: 10.1016/j.apcatb.2023.122835.

75. Bojdys, M. J.; Müller, J.-O.; Antonietti, M., et al. *Chem. Eur. J.* **2008**, 14 (27), 8177–8182. DOI: 10.1002/chem.200800190.

76. Toledo, R. R.; Santoyo, V. R.; Sánchez, D. M., et al. *Nova scientia* **2018**, 10 (1), 83–99. DOI: 10.21640/ns.v10i20.1217.

77. Lai, S.-H.; Chen, Y.-B.; Li, N., et al. *J. Mater. Sci.: Mater. Electron.* **2018**, 29 (6), 4509–4516. DOI: 10.1007/s10854-017-8399-8.

78. Köwitsch, I.; Mehring, M. *J. Mater Sci* **2021**, 56 (33), 18608–18624. DOI: 10.1007/s10853-021-06405-z.

79. Lau, V. W.; Lotsch, B. V. *Adv. Eng. Mater.* **2022**, 12 (4). DOI: 10.1002/aenm.202101078.

80. Wang, W.; Kou, X.; Zhao, R., et al. *J. Nanopart. Res.* **2021**, 23 (4). DOI: 10.1007/s11051-021-05168-7.

81. Zhang, K.; Liu, C.; Liu, Q., et al. *Catalysts* **2023**, 13 (4), 717. DOI: 10.3390/catal13040717.

82. Yan, X.; Ning, G.; Zhao, P. *Catalysts* **2019**, 9 (1), 55. DOI: 10.3390/catal9010055.

83. Fina, F.; Callear, S. K.; Carins, G. M., et al. *Chem. Mater.* **2015**, 27 (7), 2612–2618. DOI: 10.1021/acs.chemmater.5b00411.

84. Villalobos, L. F.; Vahdat, M. T.; Dakhchoune, M., et al. *Sci. Adv.* **2020**, 6 (4), eaay9851. DOI: 10.1126/sciadv.aay9851.

85. Cherepanova, S. V.; Tsybulya, S. V. *Mater. Sci. Forum (Materials Science Forum)* **2004**, 443-444, 87–90. DOI: 10.4028/www.scientific.net/MSF.443-444.87.

86. Niu, P.; Zhang, L.; Liu, G., et al. *Adv. Funct. Materials.* **2012**, 22 (22), 4763–4770. DOI: 10.1002/adfm.201200922.

87. Dillip, G. R.; Sreekanth, T.; Joo, S. W. *Ceram. Int.* **2017**, 43 (8), 6437–6445. DOI: 10.1016/j.ceramint.2017.02.057.

88. Challagulla, S.; Payra, S.; Chakraborty, C., et al. *Phys. Chem. Chem. Phys.* **2019**, 21 (6), 3174–3183. DOI: 10.1039/c8cp06855k.

89. Chen, Y.; Yang, Y.; Wang, W., et al. *J. Mater. Sci.: Mater. Electron.* **2022**, 33 (9), 6190–6200. DOI: 10.1007/s10854-022-07794-w.

90. Saner, B.; Okyay, F.; Yürüm, Y. *Fuel* **2010**, 89 (8), 1903–1910. DOI: 10.1016/j.fuel.2010.03.036.

91. Jerigova, M.; Markushyna, Y.; Teixeira, I. F., et al. *Adv. Sci.* **2023**, 10 (13), e2300099. DOI: 10.1002/advs.202300099.

92. Chantler, C. T.; Bunker, G.; D'Angelo, P., et al. *Nat. Rev. Methods Primers (Nature Reviews Methods Primers)* **2024**, 4 (1). DOI: 10.1038/s43586-024-00366-8.

93. Mo, Z.; Di, J.; Yan, P., et al. *Small* **2020**, 16 (48). DOI: 10.1002/smll.202003914.

94. Mo, Z.; Zhu, X.; Jiang, Z., et al. *Appl. Catal. B: Environ.* **2019**, 256, 117854. DOI: 10.1016/j.apcatb.2019.117854.

95. Pérez-Torres, A. F.; Hernández-Barreto, D. F.; Bernal, V., et al. *ACS Omega* **2023**, 8 (50), 47821–47834. DOI: 10.1021/acsomega.3c06320.

96. Zhang, J.-R.; Ma, Y.; Wang, S.-Y., et al. *Phys. Chem. Chem. Phys.* **2019**, 21 (41), 22819–22830. DOI: 10.1039/c9cp04573b.

97. Han, C.; Su, P.; Tan, B., et al. *J. Colloid Interface Sci.* **2021**, 581 (Pt A), 159–166. DOI: 10.1016/j.jcis.2020.07.119.

98. Yang, X.; Qian, F.; Zou, G., et al. *Appl. Catal. B: Environ.* **2016**, 193, 22–35. DOI: 10.1016/j.apcatb.2016.03.060.

99. Zhang, G.; Wu, Z.; Liu, H., et al. *Small* **2017**, 13 (41). DOI: 10.1002/smll.201702225.

100. Lan, Y.; Li, Z.; Li, D., et al. *Appl. Surf. Sci.* **2019**, 467-468, 411–422. DOI: 10.1016/j.apsusc.2018.10.152.

101. Zhang, J.; Li, X.; Zheng, J., et al. *Process Saf. Environ. Prot.* **2024**, 190, 1105–1113. DOI: 10.1016/j.psep.2024.08.010.

102. Karjule, N.; Rana, M.; Shalom, M., et al. *Adv. Sust. Sys.* **2021**, 5 (3). DOI: 10.1002/adsu.202000265.

103. Lin, L.; Lin, Z.; Zhang, J., et al. *Nat. Catal.* **2020**, 3 (8), 649–655. DOI: 10.1038/s41929-020-0476-3.

104. Teng, X.; Ma, C.; Ge, C., et al. *J. Mater. Chem. B* **2014**, 2 (29), 4631–4639. DOI: 10.1039/c4tb00368c.

105. Qian, X.; Li, N.; Imerhasan, M., et al. *Colloids Surf. A: Physicochem. Eng. Asp.* **2019**, 573, 255–261. DOI: 10.1016/j.colsurfa.2019.04.037.

106. Pietrowski, M.; Alwin, E.; Zieliński, M., et al. *Nanoscale Adv.* **2024**, 6 (6), 1720–1726. DOI: 10.1039/d3na00983a.

107. Ng, B.-J.; Putri, L. K.; Chong, W.-K., et al. *J. Mater. Chem. A* **2024**, 12 (36), 23971–24004. DOI: 10.1039/D4TA03163F.

108. Yang, P.; Wang, R.; Zhou, M., et al. *Angew. Chem.* **2018**, 57 (28), 8674–8677. DOI: 10.1002/anie.201804996.

109. Li, Q.; Zhao, S.; Jiang, B., et al. *Mater. Today* **2024**, 80, 886–904. DOI: 10.1016/j.mattod.2024.09.019.

110. Pendyala, V. R. R.; Jacobs, G.; Ma, W., et al. *Catal. Lett.* **2016**, 146 (10), 1858–1866. DOI: 10.1007/s10562-016-1820-8.

111. Zhang, J.; Gao, M.; Wang, R., et al. *Nano Res.* **2023**, 16 (4), 4786–4792. DOI: 10.1007/s12274-022-5260-z.

112. Ribeiro, M. Z. L. L.; Souza, J. C.; Gomes, I. F., et al. *Catalysts* **2024**, 14 (10), 682. DOI: 10.3390/catal14100682.

113. Lyu, S.; Wang, J.; Zhou, Y., et al. *Adv. Funct. Materials (Advanced Functional Materials)* **2024**, 34 (10). DOI: 10.1002/adfm.202310286.

114. Cesano, F.; Cravanzola, S.; Brunella, V., et al. *Front. Mater.* **2019**, 6. DOI: 10.3389/fmats.2019.00084.

115. Pimenta, M. A.; Dresselhaus, G.; Dresselhaus, M. S., et al. *Phys. Chem. Chem. Phys.* **2007**, 9 (11), 1276–1291. DOI: 10.1039/b613962k.

116. Ferrari, A. C.; Robertson, J. *Phys. Rev. B Condens.* **2000**, 61 (20), 14095–14107. DOI: 10.1103/PhysRevB.61.14095.

117. Rivas-Murias, B.; Salgueiriño, V. *J. Raman Spectroscopy* **2017**, 48 (6), 837–841. DOI: 10.1002/jrs.5129.

118. Lazzarini, A.; Piovano, A.; Pellegrini, R., et al. *Catal. Sci. Technol.* **2016**, 6 (13), 4910–4922. DOI: 10.1039/C6CY00159A.

119. Thomsen, C.; Reich, S. *Physical review letters* **2000**, 85 (24), 5214–5217. DOI: 10.1103/PhysRevLett.85.5214.

120. Ferrari, A. C.; Robertson, J. *Philos. Trans. A Math. Phys. Eng. Sci.* **2004**, 362 (1824), 2477–2512. DOI: 10.1098/rsta.2004.1452.

121. Maldonado, S.; Morin, S.; Stevenson, K. J. *Carbon* **2006**, 44 (8), 1429–1437. DOI: 10.1016/j.carbon.2005.11.027.

122. Maślana, K.; Kaleńczuk, R. J.; Zielińska, B., et al. *Materials* **2020**, 13 (6). DOI: 10.3390/ma13061349.

123. Sharifi, T.; Nitze, F.; Barzegar, H. R., et al. *Carbon* **2012**, 50 (10), 3535–3541. DOI: 10.1016/j.carbon.2012.03.022.

124. Falbo, L.; Visconti, C. G.; Lietti, L., et al. *Appl. Catal. B: Environ.* **2019**, 256, 117791. DOI: 10.1016/j.apcatb.2019.117791.

125. Proaño, L.; Tello, E.; Arellano-Trevino, M. A., et al. *Appl. Surf. Sci.* **2019**, 479, 25–30. DOI: 10.1016/j.apsusc.2019.01.281.

126. Franken, T.; Terreni, J.; Borgschulte, A., et al. *J. Catal.* **2020**, 382, 385–394. DOI: 10.1016/j.jcat.2019.12.045.

127. Schreiter, N.; Kirchner, J.; Kureti, S. *Catal. Commun.* **2020**, 140, 105988. DOI: 10.1016/j.catcom.2020.105988.

128. Ni, T.; Zhang, H.; Zhou, L., et al. *Chin. Chem. Lett.* **2025**, 36 (9), 110659. DOI: 10.1016/j.cclet.2024.110659.

129. Park, J.; Zafar, F.; Kim, C. H., et al. *Fuel Process. Technol.* **2019**, 184, 36–44. DOI: 10.1016/j.fuproc.2018.11.001.

130. Liu, Y.; Niu, X.; Yang, X., et al. *Chem. Eng. J.* **2024**, 489, 151417. DOI: 10.1016/j.cej.2024.151417.

131. Nyathi, T. M.; Fischer, N.; York, A. P. E., et al. *ACS Catal.* **2019**, 9 (8), 7166–7178. DOI: 10.1021/acscatal.9b00685.

132. Mo Koo, H.; Wang, X.; Rong Kim, A., et al. *Fuel* **2021**, 287, 119437. DOI: 10.1016/j.fuel.2020.119437.

133. Negro, P.; Cesano, F.; Casassa, S., et al. *Materials* **2023**, 16 (10), 3644. DOI: 10.3390/ma16103644.